

Alma Mater Studiorum Università di Bologna  
Archivio istituzionale della ricerca

Geothermometric Constraints on the Thermal Architecture, Metamorphism, and Exhumation of the Northern Range, Trinidad

This is the final peer-reviewed author's accepted manuscript (postprint) of the following publication:

*Published Version:*

Gennaro, I., Weber, J., Vitale Brovarone, A., Arkle, J., Chu, X.u. (2022). Geothermometric Constraints on the Thermal Architecture, Metamorphism, and Exhumation of the Northern Range, Trinidad. JOURNAL OF METAMORPHIC GEOLOGY, 41, 1-23 [10.1111/jmg.12697].

*Availability:*

This version is available at: <https://hdl.handle.net/11585/905011> since: 2023-03-01

*Published:*

DOI: <http://doi.org/10.1111/jmg.12697>

*Terms of use:*

Some rights reserved. The terms and conditions for the reuse of this version of the manuscript are specified in the publishing policy. For all terms of use and more information see the publisher's website.

This item was downloaded from IRIS Università di Bologna (<https://cris.unibo.it/>).  
When citing, please refer to the published version.

(Article begins on next page)

This is the final peer-reviewed accepted manuscript of:

Gennaro, Ivano; Weber, John; Vitale Brovarone, Alberto; Arkle, Jeanette; Chu, Xu:  
*Geothermometric Constraints on the Thermal Architecture, Metamorphism, and  
Exhumation of the Northern Range, Trinidad*

JOURNAL OF METAMORPHIC GEOLOGY vol. 41 ISSN 0263-4929

DOI: 10.1111/jmg.12697

The final published version is available online at:

<https://dx.doi.org/10.1111/jmg.12697>

Terms of use:

Some rights reserved. The terms and conditions for the reuse of this version of the manuscript are specified in the publishing policy. For all terms of use and more information see the publisher's website.

This item was downloaded from IRIS Università di Bologna (<https://cris.unibo.it/>)

**When citing, please refer to the published version.**

**Geothermometric Constraints on the Thermal Architecture, Metamorphism, and Exhumation of  
the Northern Range, Trinidad**

Ivano Gennaro<sup>1\*†</sup>, John Weber<sup>2</sup>, Alberto Vitale Brovarone<sup>3, 4, 5</sup>, Jeanette Arkle<sup>6</sup>, Xu Chu<sup>1</sup>

<sup>1</sup> Department of Earth Sciences, University of Toronto. Toronto, Ontario M5S 3B1, Canada

<sup>2</sup> Department of Geology, Grand Valley State University. Allendale, Michigan 49401, USA

<sup>3</sup> Dipartimento di Scienze Biologiche, Geologiche e Ambientali, Alma Mater Studiorum Università di Bologna, Bologna, Italy.

<sup>4</sup> Sorbonne Université, Museum National d'Histoire Naturelle, UMR CNRS 7590, IRD, Institut de Minéralogie, des Physique de Matériaux et de Cosmochimie, Paris, France

<sup>5</sup> Institute of Geosciences and Earth Resources, National Research Council of Italy, Pisa, Italy

<sup>6</sup> Department of Geology, Augustana College, Rock Island, IL 61201, USA

\*Ivano Gennaro: [ivanogennaro@gmail.com](mailto:ivanogennaro@gmail.com); <https://orcid.org/0000-0002-9903-781X>

John Weber: [weberj@gvsu.edu](mailto:weberj@gvsu.edu)

Alberto Vitale Brovarone: [alberto.vitaleb@unibo.it](mailto:alberto.vitaleb@unibo.it)

Jeanette Arkle: [jennyarkle@augustana.edu](mailto:jennyarkle@augustana.edu); <https://orcid.org/0000-0003-0640-6178>

Xu Chu: [xu.chu@utoronto.ca](mailto:xu.chu@utoronto.ca); <https://orcid.org/0000-0002-6816-1076>

† Current institute: Département de Sciences de la Terre, Université de Genève, 1205 Genève, Switzerland

27    **Running Title**

28    Thermal architecture of the Northern Range

29

30    **Keywords**

31    RSCM geothermometry, Trinidad, Geothermometry, Caribbean tectonics

32

33    **Data Availability**

34            The data presented here as supplemental material (Tables S1 and S2) are openly available on the  
35    PANGAEA Database and may be accessed under the DOI:  
36    <https://doi.pangaea.de/10.1594/PANGAEA.932772>

37

## 38    **Abstract**

39            The Northern Range of Trinidad is composed of Mesozoic passive margin sedimentary rocks  
40    that underwent ductile deformation and sub-greenschist to greenschist facies metamorphism in the early  
41    Miocene. Previous studies identified a westward increase in the metamorphic grade but were unable to  
42    resolve whether this trend was discrete or continuous. In this study, we use Raman spectroscopy on  
43    carbonaceous materials (RSCM) to constrain peak temperatures across the Northern Range with a  
44    greater resolution than was available in previous studies. These data are then combined with published  
45    thermochronological data to constrain the tectonic history of a range-cutting fault that had been  
46    previously inferred in previous geologic mapping. The RSCM temperatures show an abrupt increase  
47    from  $337 \pm 10$  °C in the east to  $442 \pm 16$  °C west of the Chupara Fault at Chupara Point. Our RSCM-  
48    derived peak metamorphic temperatures are 50–100 °C higher than those from previous estimates,  
49    requiring revision of tectonic models to account for deeper burial and greater exhumation. The peak  
50    metamorphic conditions determined here, and our inferred timing of faulting, are consistent with the  
51    two-stage tectonic model proposed in previous studies. A two-sided wedge formed during oblique plate  
52    collision and mountain building (stage I). Cooling rates differed in the Northern Range between eastern  
53    and western blocks between ~10–4.5 Ma; this difference is attributed here to the activity along the cross-  
54    range Chupara Fault. This pattern of differential cooling, bedrock exhumation, and inferred bedrock and  
55    surface uplift may be associated with plate-scale strike-slip tectonics and the passage of a crustal-scale  
56    bulge induced by deep tearing of South American lithosphere (stage II).

57

## 58 1. INTRODUCTION

59           Trinidad, the largest island in the nation of Trinidad and Tobago, is the southeastern-most island  
60 in the Caribbean and is located in the Caribbean-South American plate boundary zone (Fig. 1a), where  
61 the Caribbean plate currently moves east relative to the South American Plate at a rate of ~20 mm/yr  
62 (Weber, Dixon, et al., 2001). Current dextral plate motion is accommodated primarily along the Central  
63 Range Fault, which strikes NEE-SWW through the middle of the island (Weber, 2009; Weber, Dixon, et  
64 al., 2001). The Northern Range, composed of Mesozoic passive margin sedimentary rocks that were  
65 metamorphosed in the early Neogene, exposes pre-transform tectonic structures. Plate convergence in  
66 the early Miocene gave rise to shortening in the foreland fold-and-thrust belt and metamorphism at sub-  
67 greenschist to greenschist facies conditions in the Northern Range segment of the hinterland belt (Algar  
68 & Pindell, 1993; Frey et al., 1988; Weber, Ferrill, et al., 2001). Following the culmination of contraction  
69 and burial, exhumation of the hinterland metamorphic rocks took place from the Miocene to Pliocene,  
70 which is thought to have resulted from an oblique Caribbean-South American Plate collision (Algar &  
71 Pindell, 1993; Weber, Ferrill et al., 2001) and/or propagation of a deep-seated lithospheric tear fault  
72 (Arkle et al., 2017, 2021; Clark et al., 2008). The post-peak-metamorphic structures of the Northern  
73 Range preserve the history of the regional exhumation kinematics (Weber, Ferrill et al., 2001), but the  
74 general low grade of the Northern Range rocks limits the utility of conventional geothermometers for  
75 accurately assessing metamorphic conditions and changes. Illite crystallinity measurements, carbonate  
76 thermometry, muscovite-paragonite geothermometry, and mineral equilibria were used to establish  
77 baseline metamorphic conditions (Frey et al., 1988; Weber, Ferrill, et al., 2001). Using temperature-  
78 sensitive quartz and calcite microstructures, Weber, Ferrill, et al. (2001) were the first to recognize a  
79 systematic increase in deformation temperatures from east to west. However, this method involved high

80 uncertainties in temperature estimates, making it difficult to identify whether this temperature gradient is  
81 continuous or segmented by discrete structures.

82 Raman spectroscopy on carbonaceous material (RSCM) is applicable to a wide range of  
83 lithologies within metamorphic terranes; it is particularly powerful in resolving low-grade peak  
84 metamorphic temperatures, such as those in the Northern Range. This geothermometric technique  
85 utilizes the crystallinity of carbonaceous material (CM) within the temperature range of 150–650 °C  
86 (Aoya et al., 2010; Beyssac et al., 2002; Kouketsu et al., 2014; Lahfid et al., 2010). With increasing  
87 metamorphic temperatures, amorphous CM evolves towards turbostratic carbon and then graphitic  
88 carbon through the process of graphitization, which is reflected in the relative areas of graphite and  
89 defect bands in Raman spectra (Beyssac & Lazzeri, 2012; Beyssac et al., 2002; Lahfid et al., 2010;  
90 Wopenka & Pasteris, 1993). Because graphitization is theorized to be an irreversible process, the  
91 crystallinity and Raman spectra of the CM should record peak metamorphic temperature conditions  
92 (Beyssac & Lazzeri, 2012; Beyssac et al., 2003). It is important to ensure quality sample collection and  
93 preparation for RSCM analysis, as for example, brittle deformation can affect the CM structure and  
94 therefore the calculated metamorphic temperatures (Nakamura et al., 2015; Kirlova et al., 2018). When  
95 high-resolution RSCM is combined with a high sample density this geothermometer can identify  
96 structural features not seen using less accurate methods (e.g., see Fig. 3 of Vitale Brovarone & Agard,  
97 2013). The technique has been applied in a variety of metamorphic environments, from high-pressure  
98 terranes to contact aureoles (Bayet et al., 2018; Beyssac et al., 2019; Lahfid et al., 2010; Molli et al.,  
99 2018; Rahl et al., 2005; Simoes et al., 2007; Vitale Brovarone & Agard, 2013; Vitale Brovarone et al.,  
100 2013).

101 The Northern Range rocks and structures are deeply weathered, covered by dense tropical  
102 vegetation, and, aside from excellent coastal and stream exposures, are generally poorly exposed and

difficult to access. Thus, previous structural studies have produced contradicting maps and interpretations (see below). In this study, we approach some of the unsolved structural and kinematic problems from a metamorphic perspective. Specifically, we use RSCM geothermometry to determine the peak metamorphic temperatures for a robust suite of Northern Range samples from east to west across the range (Fig. 2). We aimed to resolve the field gradient and to provide new temperature constraints to better establish the thermal architecture of the Northern Range. These new constraints help us determine whether the Northern Range was exhumed as a single rigid block or as discrete, fault-bounded range segments. Our new RSCM data, combined with previously published geological maps and thermochronological data, confirm the presence of a large-scale, cross-range, crustal-scale fault, the Chupara Fault, which was previously mapped but only poorly defined. Based on our new RSCM constraints, we review and modify existing tectonic models to explain the metamorphic, emplacement, and exhumation history of the Northern Range. The results presented here explore the thermal architecture and tectonic evolution of a mountain range formed in plate boundary that transitioned from collisional to transform, providing a real-world laboratory to examine processes that can then be used to better constrain geodynamic models (e.g. Govers & Wortel, 2005).

## **2. TECTONIC FRAMEWORK AND GEOLOGIC HISTORY**

The Caribbean plate is postulated to have developed from the Caribbean large igneous province, an oceanic plateau or hotspot swell that formed from 139–83 Ma far west of its current location (Burke, 1988; Hoernle et al., 2004). The Caribbean plate began migrating eastward and entered the gap between the North and South American plates near the end of the Cretaceous (~66 Ma), and it eventually collided with northwestern South America (Kennan & Pindell, 2009) and southern North America. The rocks of the Northern Range were presumably derived from passive margin sediments deposited along the



126 northern edge of South America (Frey et al., 1988; Robertson & Burke, 1989). These sedimentary rocks  
127 underwent low-grade metamorphism, with sub-greenschist mineral assemblages present in the east and  
128 greenschist assemblages present in the central and western Northern Range (Frey et al., 1988, Weber,  
129 Ferrill, et al., 2001). The presence of slates, marbles, quartzite and schists, as well as their detrital zircon  
130 U-Pb age spectra, supports a passive margin provenance for these rocks (Bartlett et al., 2021).

131 Zircon fission-track thermochronology data was used to suggest that the initial phase of  
132 metamorphism and deformation in the Northern Range may have started as early as the late Eocene  
133 (Algar & Pindell, 1993), but this interpretation was based on partially reset samples and from only a  
134 limited portion of the range. Subsequent studies used apatite fission track and apatite and zircon (U-  
135 Th)/He data to revealed that the initial exhumation of the Northern Range occurred ~10–8 Ma in west  
136 and ~6–4 Ma in the east (Arkle et al., 2021). Hinterland structural and metamorphic events are most  
137 clearly delineated in the western Northern Range. White mica  $^{40}\text{Ar}/^{39}\text{Ar}$  ages date peak metamorphism  
138 in the Northern Range between 23 Ma and 34 Ma (Foland et al., 1992; Speed et al., 1997; Weber &  
139 Arkle, 2015). Syn-metamorphic deformation (isoclinal  $F_1$  folding, transposition of original bedding, and  
140  $S_1$  foliation development) was followed by a second  $F_2$  folding event and the development of  $S_2$   
141 crenulation cleavage (Weber, Ferrill, et al., 2001). The general picture is that plate-scale transpression  
142 drove high magnitude crustal shortening and exhumation in the southern Caribbean metamorphic  
143 hinterland, which includes the Northern Range (Cruz et al., 2007; Weber, Ferrill, et al., 2001). The main  
144 stages of deformation and exhumation in the hinterland belt are largely coeval with folding and thrusting  
145 in the Trinidad foreland, i.e., the Central and Southern Ranges. Deformation and exhumation in the  
146 Central Range is constrained to have occurred in the mid-Miocene (11–18 Ma) by using stratigraphy and  
147 zircon (U-Th)/He dating (Giorgis et al., 2017).

148 A late stage of deformation ( $D_3$ ) within the Northern Range is recorded as a series of steeply

149 dipping normal faults that strike SE-NW and NE-SW and crosscut previous fabric elements (Fig. 2;  
150 Kugler, 1961; Weber, Ferrill, et al., 2001). These faults have been interpreted as related to E-W  
151 transform shear, and as such, these faults may accommodate transtension associated with relative  
152 Caribbean-South American strike-slip motion (Algar & Pindell, 1993). Thus, Flinch et al. (1999) posit  
153 that these D<sub>3</sub> faults formed during or after the late Miocene or Pliocene.

154         Many different scenarios have been proposed to explain the metamorphism and exhumation of  
155 the metamorphic hinterland belt along northern South America. A few works advocate for the oblique  
156 collision and subduction of South America beneath the Caribbean plate (Audemard, 2009; Cruz et al.,  
157 2007; Pindell & Kennan, 2001, 2007, 2009). Some oblique collision models require about 240 km of  
158 displacement since 12 Ma to bring the Northern Range into its current position (Pindell & Kennan,  
159 2001). Exhumation of the Northern Range has been explained by isostatic rebound after forming a deep  
160 crustal root that developed during an oblique collision (Algar & Pindell, 1993; Algar et al., 1998; Cruz  
161 et al., 2007), or through the activation of late-stage, range-bounding brittle structures. Weber, Ferrill, et  
162 al. (2001), for instance, initially called on differential dip-slip along the Arima Fault, a late south-side-  
163 down normal fault bounding the southern Northern Range (Fig. 1b & 2), to explain differences in  
164 eastern and western metamorphic grades.

165         Alternatively, metamorphism, deformation, and exhumation of the Northern Range could be  
166 associated with the passage of a lithospheric tear fault under Trinidad (Arkle et al., 2017, 2021; Clark et  
167 al., 2008; Levander et al., 2014). Currently, the subduction of the Atlantic oceanic lithosphere (of both  
168 the North and South American plates) under the Caribbean plate is accommodated by tearing of the  
169 lithosphere along a subduction-transform edge propagator (STEP, Fig. 1c; Govers and Wortel, 2005).  
170 STEP faults mark the transition between subduction and transform plate boundaries and are  
171 characterized by non-uniform relative plate motion; deformation, rotation, and uplift are often induced

172 along the transform side of the transition as the subducting plate is torn at the STEP edge (Govers &  
173 Wortel, 2005). The active southeastern Caribbean STEP fault is marked by the Paria cluster of depth  
174 earthquakes beneath the northern coast of eastern Venezuela (Fig. 1a), and the active STEP edge is  
175 currently proposed to be positioned offshore eastern Trinidad, about 175 km east of the Paria cluster (c.f.  
176 Fig. 2 of Nijholt & Govers, 2015). Some recent interpretations have postulated that exhumation of the  
177 Northern Range was driven by STEP fault processes including the detachment of the South American  
178 lithosphere, asthenosphere flow, and flexural bulging ahead of the STEP tear (Arkle et al., 2017; 2021;  
179 Clark et al., 2008; Levander et al., 2014). Accordingly, eastward propagation of the Caribbean plate and  
180 associated STEP fault caused the observed asymmetric exhumation, and the thermochronological ages  
181 from the region that increase eastward and post-date the presumed oblique collision (Arkle et al., 2021).  
182 STEP-induced deformation also fits the observed Quaternary tectonic inversion and asymmetry of slow  
183 eastern and fast western exhumation rates (Arkle et al., 2017; Clark et al., 2008; Levander et al., 2014).  
184 Differences between regional tectonic models germane to this study are whether the hinterland  
185 metamorphic rocks are allochthonous and disconnected with folding and thrusting in the foreland or  
186 parautochthons and connected with foreland deformation in space and time.

187

### 188 **3. GEOLOGIC SETTING AND SAMPLE DESCRIPTION**

#### 189 **3.1 Structures and Stratigraphy**

190 The Northern Range of Trinidad is bounded by the Arima Fault to the south and the Northern  
191 Coast and Sub-Tobago Terrane faults offshore to the north (Fig. 1b) (Robertson and Burke, 1989; Weber  
192 et al. 2015, 2020). The Arima Fault was originally mapped by Kugler (1961) and corresponds to  
193 observable meso-scale faults and cataclastic zones (Weber, Ferrill et al., 2001). Previously hypothesized

194 to be an eastward extension of the El Pilar transform fault, the Arima Fault is actually a south-side-  
195 down, inactive normal fault that accommodated N–S extension (Weber, Ferrill et al., 2001). The  
196 subsurface Caroni fault may instead represent the eastern El Pilar extension (Pindell & Kennan, 2007),  
197 though active strike-slip motion now occurs along the Central Range Fault to the south (Fig. 1b; Weber,  
198 Dixon, et al., 2001). The North Coast and Sub-Tobago Terrane fault zones (Fig. 1b) accommodate active  
199 strike-slip and normal dip-slip between the Northern Range and Tobago terrane (Robertson & Burke,  
200 1989; Weber et al. 2015, 2020). This offshore fault zone also contains *en echelon* normal faults that  
201 strike northwest and have moderate to steep northeastern dips (Robertson & Burke, 1989). These *en*  
202 *echelon* structures mirror the late normal faults mapped and observed in the Northern Range at the  
203 meso- and macro-scales (Fig. 2) and are attributed by Robertson & Burke (1989) to be related to broad,  
204 plate-scale, transform shear. Such structures are also mapped in eastern Paria (Cruz et al., 2007).

205 At Chupara Point, both Kugler (1961) and De Verteuil et al. (2005) infer the presence of the  
206 Chupara Fault, a northwest-striking, steeply dipping, west-side-up normal fault. The inferred Chupara  
207 Fault trends NNW-SSE from Chupara Point on the north coast, across the range, potentially extending  
208 across the entire range southward to where it is truncated by the Arima Fault near the town of Maturita  
209 (Fig. 2; Kugler, 1961; De Verteuil et al., 2005). On the other hand, Potter (1968) inferred a series of  
210 short, disconnected, NW-striking fault segments at Chupara Point, Verdant Vale, and along the southern  
211 foot of the range. Kugler (1961) mapped the Chupara Fault as one in a series of southeast- and  
212 southwest-striking normal faults. Some of the other geologic maps of the range do not show the Chupara  
213 Fault (e.g., Saunders et al., 1997). Mapping the Northern Range has been a significant challenge.  
214 Kugler's (1961) biostratigraphic approach that proved so successful in Trinidad's sedimentary rocks  
215 further south, together with related attempts to establish a protolith stratigraphy in these metamorphic  
216 rocks, has largely failed (see below).

217           The metasedimentary rocks of the Northern Range include predominantly slates, quartz and mica  
218 schists, quartzites, and metacarbonates. Mesozoic fossils have been reported from only about a dozen  
219 localities scattered in the range (e.g., Dighton-Thomas, 1935; Imlay, 1954; Kugler, 1961; Saunders,  
220 1972; Spath, 1939; Trechmann, 1935); these ages range from Tithonian (Jurassic) (?) to Maastrichtian  
221 (Upper Cretaceous) (Fig. 2). Significantly, relict fossils have only been found in the low-grade rocks  
222 east of the inferred Chupara Fault and in the fault-bounded, low-grade Laventille metalimestone and  
223 Lopinot phyllite along the range front. Apparently, no relict fossils have survived in the higher-grade  
224 metamorphism west of the Chupara Fault, which have been isoclinally folded, structurally transposed  
225 (i.e., original bedding has been rotated into, cut by, and highly stretched in the  $S_1$  foliation), and highly  
226 recrystallized. In addition to the relict fossils, two radiometric ages that are highly disparate have been  
227 reported from the San Souci metabasalt, which is a small and significant, but poorly studied, poorly  
228 mapped, and poorly understood meta-igneous unit in the range (Fig. 2). Wadge & Macdonald (1985)  
229 report a whole rock K-Ar protolith age of  $87 \pm 4.4$  Ma, whereas Neill et al. (2014) dismiss the earlier  
230 age as erroneous due to alteration and report a  $135 \pm 7.3$  Ma zircon U-Pb crystallization age.

231           Traditionally it has been assumed, though not demonstrated, that a simple protolith stratigraphy  
232 still exists in these metamorphic formations, despite the limitations discussed above, and the fact that  
233 they are indeed metamorphic rocks, not sedimentary rocks (Algar & Pindell, 1993; Barr, 1965; Kugler,  
234 1961; Potter, 1973; Saunders, 1997). Even in the western Northern Range, where relict fossils are  
235 completely absent, this imagined protolith stratigraphy leads to the erroneous, widespread, and still  
236 recently circulating interpretation that the megastructure of the Northern Range is a northward-vergent,  
237 overturned, macroscopic anticline (Kugler, 1961; Potter, 1973; Algar and Pindell, 1993; Babb & Mann,  
238 1999). Instead, the sheet dip of the bedding-parallel  $S_1$  foliation is consistently toward the south there  
239 and forms a homocline in which the resistant metamorphic units (quartz schists and quartzites) form a

240 series of south-dipping dip-slopes and hogbacks. The De Verteuil et al. (2005) map is the first attempt to  
241 abandon the hypothesized protolith stratigraphy and simply map metamorphic rock types as directly  
242 observed in the field. We follow a similar approach below as we describe and treat the units in the  
243 Northern Range as low-grade metamorphic terranes.

### 244 **3.2 Petrography and Sample Descriptions**

245 Northern Range protoliths were likely derived from passive margin sediments deposited along  
246 the northern edge of South America during and after the breakup of Pangea in the Jurassic and  
247 throughout the Cretaceous (Speed, 1985; Frey et al., 1988; Robertson & Burke, 1989; Bartlett et al.,  
248 2021). These protoliths were likely carbonates, mudstones, and sandstones, which have been  
249 metamorphosed at sub-greenschist to greenschist facies conditions (Frey et al., 1988). The protoliths  
250 represent a mixture of continental shelf sedimentary rocks that were deformed and exhumed during and  
251 after Miocene collision (Pindell & Kennan, 2001, 2007). The twenty-six samples we collected and  
252 analyzed are representative of the six major lithologies from across the Northern Range (Fig. 2) (1)  
253 high-grade, foliated marble, (2) low-grade metacarbonate, (3) mica schist, (4) mica-rich phyllite, (5)  
254 metasandstone, and (6) carbon-rich slate (Fig. 2 & 3).

255 The high-grade marbles (Fig. 3a) are all strongly foliated, exhibiting dark bands rich in CM and  
256 lighter, carbonate-rich bands. Many of these samples also contain minor sulfides, mainly pyrite and  
257 arsenopyrite; some of the pyrite grains have been weathered and broken down into iron oxides. The low-  
258 grade metacarbonates (Fig. 3b; metacarbonate in Fig. 2) generally preserve primary sedimentary  
259 structures and textures (Fig. 3c). Fossil shells and ooids are common in many of these rocks, which  
260 exhibit low-strain, ductile deformation at the micro-scale (Fig. 3c). Some low-grade metacarbonates are  
261 crosscut by calcite-filled veins indicative of brittle extensional deformation and precipitation from  
262 metamorphic fluids. Further, later stage brittle deformation is recorded by the cross-cutting of calcite

263 veins by fractures.

264         The quartz-mica schists (Fig. 3d) mainly crop out in the western Northern Range. These schists  
265 are well-foliated and consist of a greenschist-facies mineral assemblage (muscovite + chlorite + quartz +  
266 plagioclase + CM  $\pm$  biotite  $\pm$  oxides or sulfides). These rocks are variable in both composition and  
267 structure, showing a wide range of mica content (5–25%). Coarser-grained rocks tend to have less mica  
268 and a less evident foliation. These are the only rocks seen to host metamorphic biotite in substantial  
269 quantities, indicating they are likely of the highest grade in the study area. Quartz and calcite grains in  
270 these rocks are thermally recrystallized, as indicated by the presence of undulose extinction in quartz  
271 and the presence of triple-point grain boundaries (Fig. 3d). Recrystallization likely occurred during  
272 deformation, as evidenced by the oriented stretching elongation of quartz parallel to the  $S_1$  foliation  
273 plane (Fig. 3d). This elongation is consistent with the observations of Weber, Ferrill, et al. (2001), who  
274 attributed the foliation to the first stage,  $D_1$ , of Northern Range deformation. At the microscopic scale,  
275 CM is observed to be concentrated in mica-rich bands related to the tight  $F_1$  folds that transpose bedding  
276 ( $S_0$ ) into  $S_1$  and later kink bands.

277         The phyllites (Fig. 3e) are extremely rich in sericite, and are fine-grained, and well foliated. The  
278 phyllitic foliation is defined by sericite  $\pm$  chlorite, with some degree of post- $S_1$  crenulation common in  
279 these rocks. The multiple foliation planes recorded in these phyllites reflect the first two phases of  
280 Northern Range deformation, which predominantly occurred in the ductile regime (Weber, Ferrill, et al.,  
281 2001). The CM content of the phyllites is variable; only a few samples had sufficient CM for RSCM  
282 analysis. Carbonaceous material with radial growth textures 0.1–0.3 mm in length is also observed in  
283 some of these rocks and it appears to be post-kinematic as it crosscuts foliation (Fig. 3f); multiple  
284 explanations are possible for their formation (cf. Luque et al., 1998; Rumble, 2014). Their composition  
285 was confirmed to be carbonaceous through electron probe microanalysis (EPMA).

286 Metasandstones are composed mainly of subangular quartz grains (Fig. 3g), but also contain  
287 minor mica and calcite along with CM. The weakly-metamorphosed rocks of this type come from the  
288 eastern and central Northern Range and are typically non-foliated to weakly foliated. Atypically strong  
289 foliation and folding were observed in sample NR-1 (Fig. 3h). Sample NR-1 (equivalent to NR-3)  
290 displays isoclinal microfolds, likely representing parasitic folds created during early semi-ductile  
291 deformation. Metasandstones from the central Northern Range display a weak foliation, but some quartz  
292 grains experienced modest shape changes, likely through a combination of pressure solution and low-  
293 temperature crystal plasticity (Weber, Ferrill, et al., 2001). Minor chlorite is seen in central Northern  
294 Range samples. However, it is generally absent in the eastern metasandstones, reflecting either a  
295 variation in composition or metamorphic grade; limited evidence suggests the former (Frey et al., 1988).

296 The dark, carbon-rich slates (Fig. 3i) are compositionally and texturally similar to the phyllites,  
297 but tend to have a lower mica content and higher content of carbonate minerals (Fig. 4a) and CM. These  
298 rocks are very fine-grained and well foliated, containing minor amounts of quartz, plagioclase, and  
299 sulfides that mainly occur as framboidal pyrite. These rocks have a well-developed, early  $S_1$  slaty  
300 cleavage that is weakly crenulated by subsequent deformation.

## 301 **4. METHODS**

### 302 **4.1 Electron Probe Microanalysis**

303 Quantitative wavelength-dispersive spectrometry and backscattered electron (BSE) imaging were  
304 carried out using a JEOL JXA-8230 electron probe microanalyzer (EPMA) at the University of Toronto.  
305 Quantitative analyses employed a 10 nA beam current, 15 kV accelerating voltage, and off-peak  
306 background corrections. The electron beam was defocused (10  $\mu\text{m}$ ) to minimize beam damage on  
307 carbonate minerals.



## 308    **4.2 RSCM Geothermometry**

309            Thin sections were polished to a thickness of ~35  $\mu\text{m}$  and made in accordance with the  
310 specifications of Beyssac et al. (2003) for RSCM analysis. Rocks were cut perpendicular to bedding or  
311 foliation planes and parallel to lineation in order to reduce within-sample heterogeneity caused by the  
312 anisotropy of CM (Beyssac et al., 2003). The carbonaceous inclusions in transparent minerals were  
313 analyzed using two Raman spectrometers: 15 samples were analyzed at the Department of Earth  
314 Sciences at the University of Turin (UNITO) in Turin, Italy, and another 18 samples were analyzed at  
315 the Royal Ontario Museum (ROM) in Toronto, Canada. Seven samples were analyzed on both  
316 spectrometers to ensure inter-instrument consistency. Only one sample (DT-93-1) was omitted due to a  
317 lack of CM.

318            Raman spectra were collected using a LabRAM HRVIS from Horiba Jobin Yvon Instruments at  
319 UNITO and a Horiba LabRAM ARAMIS micro-Raman spectrometer at the ROM. Both spectrometers  
320 were calibrated with a silicon standard and used a 532 nm solid-state neodymium laser. The lasers were  
321 dispersed using 1200 gr/mm gratings and focused on the samples using 100x objectives with a  
322 numerical aperture of 0.9. In order to avoid laser-induced heating, a low laser power (<5 mW) was used  
323 during analysis (Beyssac et al., 2003). At UNITO, no filter was required; at the ROM, the D1 or D0.6  
324 filters (10% and 25% transparency respectively) were used to ensure a laser power below 5 mW.

325            A combination of transmitted and reflected light was used to target CM located below the  
326 surface of the host minerals to avoid artificial defects induced by sample preparation (Beyssac &  
327 Lazzeri, 2012; Beyssac et al., 2003). At least 15 spectra were collected for each sample. The spectral  
328 baselines were corrected, and the spectra were fitted using the Peakfit software (AISN Software Inc.,  
329 1995). Wherever possible, a linear baseline was used for the correction, but micaceous samples

330 sometimes required a best-fit baseline correction as the fluorescence of mica is detectable within the  
331 range of 700–2000  $\text{cm}^{-1}$  (Beyssac & Lazzeri, 2012).

332 For samples showing CM Raman spectra characteristic of high-temperature conditions ( $>330\text{ }^{\circ}\text{C}$ ;  
333 e.g., SC-2b, Fig. 5a), we apply the 532 nm laser-based calibration of Aoya et al. (2010) (Eq. 1) along  
334 with the 514 nm laser-based calibration of Beyssac et al. (2002) (Eq. 2) as a reference. These spectra  
335 were fitted with three bands and Voigt peaks, which converged to a unique solution (Beyssac & Lazzeri,  
336 2012; Lahfid et al., 2010). For samples showing CM Raman spectra characteristic of low-temperature  
337 conditions ( $<350\text{ }^{\circ}\text{C}$ ; e.g., T94-3, Fig. 5b), we apply the 514 nm laser-based calibration of Lahfid et al.  
338 (2010) (Eq. 3) and the two 532 nm laser-based calibrations of Kouketsu et al. (2014) (Eq. 4 & 5). For the  
339 Lahfid et al. (2010) calibration, these spectra are decomposed into five bands; the use of Lorentzian  
340 profiles was necessary to reduce the degree of freedom and allow a unique solution to be obtained  
341 (Beyssac & Lazzeri, 2012; Lahfid et al., 2010). The samples were then refit following Kouketsu et al.  
342 (2014) to use their calibrations (see below). The temperatures were then calculated using the area ratios  
343 of the peaks based on the respective thermometer calibrations (see Aoya et al., 2010; Beyssac et al.,  
344 2002; Lahfid et al., 2010).

345 Most samples displayed solely high- or low-temperature spectra, whereas nine samples of  
346 intermediate temperature (300–360  $^{\circ}\text{C}$ ) feature a mixture of 3- and 5-band spectra. In the case of the  
347 nine samples with both types of spectra, the Aoya et al. (2010) calibration was applied to 3-band spectra  
348 and the Lahfid et al. (2010) calibration was applied to 5-band spectra. We note that only four reported  
349 temperatures are the averages of both calibrations that statistically overlap. The second calibration  
350 applied to the other five samples is rejected as outliers (Table 1). For example, among the fifteen  
351 datapoints of 93-T-CB, three 5-band spectra yield much lower temperatures ( $284 \pm 10\text{ }^{\circ}\text{C}$ ) than the  
352 twelve 3-band spectra which make up the majority ( $366 \pm 5\text{ }^{\circ}\text{C}$ ; Table S1). On the other hand, one

353 datapoint of MAT-1(3) shows a 3-band spectrum that yields a temperature of 472 °C, >100 °C higher  
354 than the average of the 5-band spectra ( $340 \pm 4$  °C); this CM inclusion, consistent with the temperature  
355 calculated using the Beyssac et al. (2002) calibration, is interpreted as detrital CM (Table S1). In both  
356 cases, the outliers were omitted when reporting the final temperature.

357 A second fitting of the data was done on samples with peak temperatures below 400 °C in  
358 accordance with the specifications of Kouketsu et al. (2014). These calibrations utilize 3–5 peaks which  
359 allow for the calculation of peak temperature based on the full width at half maximum (FWHM) of the  
360 D1 and D2 bands (Kouketsu et al., 2014). A second fitting ensured all spectra treated were fit with a  
361 linear baseline in the range of 1000–1750  $\text{cm}^{-1}$  with pseudo-Voigt (Gaussian-Lorentzian sum) functions  
362 in accordance with Kouketsu et al. (2014). Some peaks were fixed based on the characteristics of the  
363 Raman spectra, such as the intensity ratio of the main D and G bands, to allow for convergence to a  
364 unique solution (Kouketsu et al., 2014).

365 Following these calibrations, R2 and RA1 represent the area ratios between the main D band and  
366 the entire spectrum in high- and low-temperature samples, respectively, with  $\text{FWHM}_{\text{Dx}}$  representing the  
367 full width at half maximum of the corresponding defect band (D1 or D2) (Beyssac et al., 2002;  
368 Kouketsu et al., 2014; Lahfid et al., 2010).

369 
$$T(^{\circ}\text{C}) = 221.0(R2)^2 - 637.1(R2) + 672.3 \quad (1)$$

370 
$$T(^{\circ}\text{C}) = -445(R2) + 641 \quad (2)$$

371 
$$T(^{\circ}\text{C}) = (RA1 - 0.3758)/0.0008 \quad (3)$$

372 
$$T(^{\circ}\text{C}) = -2.15(\text{FWHM}_{\text{D1}}) + 478 \quad (4)$$

373 
$$T(^{\circ}\text{C}) = -6.78(\text{FWHM}_{\text{D2}}) + 535 \quad (5)$$

374

## 375 **5. RESULTS**

### 376 **5.1 Carbonate Thermometry**

377 Weber, Ferrill et al. (2001) presented comprehensive documentation and analyses of the calcite  
378 microstructures in the Northern Range metasedimentary rocks (see their Figure 8). Depending on the  
379 metamorphic grade, the calcite microstructures range from thin calcite twins in rocks with intact and  
380 preserved sedimentary textures to plastically deformed, fully recrystallized, mechanical twins. Given  
381 that these dynamically recrystallized calcite grains are commonly present in crosscutting veins, the  
382 highest temperatures derived from calcite microstructures in that study can thus be considered as a lower  
383 bound for peak metamorphic temperatures. Here, we attempt Ca-Mg-Fe thermometry between calcite  
384 and dolomite in a slate sample with disseminated calcite and dolomite (NR-5, equivalent to NR-2), and  
385 show that this thermometer is not applicable due to a lack of chemical and textural equilibrium.

386 A BSE image representative of the mineral assemblage and texture of NR-5 is presented in  
387 Figure 4a. Ankerite grains (dol in Fig. 4) are larger and more euhedral than calcite. The schistosity bends  
388 and forms pressure shadows around ankerite micro-porphyroblasts. The ankerite has a Mg# ( $=\text{Mg} / [\text{Mg} + \text{Fe}]$ )  $\sim 0.4$  and Ca content  $\sim 0.54$  per 3 O. The calcite contains minor ( $\sim 0.04$  per 3 O) Fe, Mg and Mn  
389 (Fig. 4b). The bending of schistosity around both calcite and ankerite grains suggests that both are likely  
390 pre-kinematic, potentially pointing to the presence of both minerals during peak metamorphism.  
391 However, the two minerals show contrasting crystal habits, with euhedral ankerite exhibiting stability  
392 while anhedral calcite grains likely reequilibrated with the surrounding matrix during retrograde  
393 metamorphism.  
394

395 Along with the disequilibrium textures, the analyzed carbonates display a high degree of  
396 scattering on the carbonate phase diagrams, yielding a large temperature range (Fig. 4b). While the  
397 thermodynamic models (Anovitz & Essene, 1987) include uncertainties and equilibrium assumptions,  
398 the variability of measured carbonate concentrations adds to the concern of applying this particular  
399 mineral-pair thermometer. Calcite microstructural geothermometry from the adjacent area yields 200–  
400 250 °C (Weber, Ferrill, et al., 2001), but inferred phase relations suggest disequilibrium between calcite  
401 and dolomite at 250 °C (Fig. 4b). In contrast to the >300 °C temperature recorded by RSCM (see  
402 below), the calcite composition and microstructures must have been modified during retrograde  
403 metamorphism. In sum, as in Frey et al. (1988), conventional geothermometers could not resolve the  
404 field gradient across the low-grade eastern Northern Range due to the violation of several of the required  
405 fundamental assumptions.

## 406 **5.2 RSCM Data and Thermometry**

407 Representative low-temperature and high-temperature Raman spectra are presented in Figure 5  
408 to illustrate the decomposition of Raman spectra for RSCM calculation. A complete set of fitted spectral  
409 data are provided in the supplementary material (Tables S1 & S2; Gennaro et al., 2021), and a complete  
410 set of results based on spectra fitting are presented in Table 1. In the first-order region (700-2000 cm<sup>-1</sup>),  
411 the low-temperature and high-temperature samples show characteristic RSCM features such as the  
412 presence of five (G, D1, D2, D3, D4) and three (G, D1, D2) major Raman bands, respectively (Fig. 5;  
413 Beyssac & Lazzeri, 2012; Beyssac et al., 2002; Lahfid et al., 2010). Samples of intermediate  
414 temperature (~340–380 °C) were also fitted with four bands in accordance with Kouketsu et al. (2014).  
415 Along with the major D and G peaks, spectra from carbonate-rich samples show calcite peaks at ~1100  
416 cm<sup>-1</sup>, which were minimized as much as possible in measurements. Values of the R<sup>2</sup> fitting correlation

417 coefficient on samples with calcite peaks may be low as this peak is removed after fitting to allow for  
418 calculations using only peaks associated with CM.

419 The centers of fitted G bands show moderate variation (Table S1; Fig. S1) from fully ordered  
420 graphite ( $1582\text{ cm}^{-1}$ ; Wang et al., 1990), especially the low-temperature samples analyzed at UNITO  
421 (Fig. S1). The downshifted Raman spectra might reflect amorphization by laser heating (Kagi et al.,  
422 1994; Iwasaki et al., 2013; Nakamura et al., 2019), as Raman spectra of low-grade CM are ideally  
423 obtained with laser powers of  $<1\text{ mW}$  to avoid laser-induced artifacts (Nakamura et al., 2019).  
424 Nonetheless, we note that the apparent temperatures calculated using 3- and 5-band calibrations (Aoya  
425 et al., 2010 and Lahfid et al., 2010, respectively) do not show any systematic correlation with the shifts  
426 of G bands (Fig. S1). Given that the intrinsic uncertainty of RSCM on low-grade samples is unquantified  
427 and potentially considerable, we reasonably regard the temperatures as robust results.

428 The temperatures from the two Kouketsu et al. (2014) calibrations display up to  $100\text{ }^{\circ}\text{C}$   
429 variations between the temperatures calculated using the two calibrations on the same sample (Fig. 6  
430 inset). The FWHM of G and D bands has been known to vary as a result of laser-induced heating at laser  
431 powers above  $1\text{ mW}$ , thus laser-induced heating is the likely cause of this discrepancy (Iwasaki et al.,  
432 2013, Nakamura et al., 2019). This is especially evident if the downshift of the G band is used as a proxy  
433 for laser-induced heating. Samples with higher scatter in the position of the G band tend to show greater  
434 disagreement between the D1- and D2-based calibrations of Kouketsu et al. (2014) (Fig. S1). Therefore,  
435 while laser-induced heating does not significantly affect the temperatures of the Aoya et al. (2010) or  
436 Lahfid et al. (2010) calibrations in our analysis, the temperatures derived from the Kouketsu et al.  
437 (2014) thermometer are considered to be significantly altered and are not used for interpretation.

438 Our new RSCM temperatures range from  $310 \pm 13\text{ }^{\circ}\text{C}$  to  $465 \pm 30\text{ }^{\circ}\text{C}$  (Lahfid et al. 2010 and  
439 Aoya et al. 2010 calibrations;  $1\sigma$ ), with an outlier at  $497 \pm 27\text{ }^{\circ}\text{C}$  (sample M-4). Figure 5c shows the

440 evolution of the acquired spectra with increasing metamorphic temperature. The spectral evolution  
441 shows an increase in the intensity ratio of the main D and G bands ( $I_D/I_G$ ) until about 350 °C, where the  
442 main G peak then begins increasing in intensity and area as the D peak decreases. In low-temperature  
443 spectra, the D3 and D4 bands decrease in area as temperature increases, and they disappear at around  
444 350 °C. Above this threshold, the D1 and D2 bands decrease in area relative to the G composite band,  
445 suggesting progressive graphitization (Beyssac et al., 2003).

446 We also assess the inter-instrument correlation between the spectra collected at UNITO and the  
447 ROM, plotting the calculated temperatures from both spectrometers against a 1:1 line (Fig. 6). The  
448 reproducibility of the high-temperature spectra is very good. However, the lower temperature spectra  
449 display a larger inter-instrument error regardless of the calibration used. A degree of inter-instrument  
450 error is to be expected, has been observed in the past, and is caused by differences in analytical settings  
451 such as laser power, the instrument's CCD, and slit spacing on the diffraction grating (Lünsdorf et al.,  
452 2013). The increased inter-instrument error in the low-temperature region may be due to differences in  
453 laser power, despite being kept below 5 mW, as laser-induced heating may still induce defects in the  
454 Raman spectrum at this energy, especially in highly amorphous CM (Beyssac et al., 2003, Kagi et al.,  
455 1994; Iwasaki et al., 2013; Nakamura et al., 2019). With regards to the scatter of low-temperature data,  
456 the calibrations for low-temperature spectra are more complex as graphitization below 330 °C is affected  
457 by variables other than just temperature (Lahfid et al., 2010). Furthermore, the RSCM calibrations,  
458 especially at low temperatures, are highly sensitive to the fitting and baseline correction method used  
459 (Beyssac & Lazzeri, 2012; Lünsdorf et al., 2013). For consistency, and to reduce the variability caused  
460 by inter-instrument error and laser-induced heating, samples from the ROM were used in all cases where  
461 samples were analyzed using both spectrometers.

462           The spatial variation of temperatures exhibits an increase from east to west across the Northern  
463 Range (Fig. 7a), in agreement with previous studies (Frey et al., 1988; Weber, Ferrill, et al., 2001). The  
464 Lahfid et al. (2010) RSCM results yield temperatures around 320 °C in the easternmost parts of the  
465 Northern Range, which increase westward to about 360 °C in the central Northern Range (Fig. 7b).  
466 Temperatures of ~360 °C in the central Northern Range are predicted by both low-temperature  
467 calibrations. An abrupt temperature difference is seen in the central Northern Range across the  
468 previously mapped Chupara Fault (De Verteuil et al. 2005; Kugler, 1961). To the west of this fault,  
469 RSCM records peak temperatures of around 450 °C, except for the two samples at ~420 °C in the  
470 vicinity of the fault. The temperature difference between the eastern ( $337 \pm 10$  °C; Lahfid et al. (2010)  
471 calibration) and western segments ( $442 \pm 16$  °C; Aoya et al. (2010) calibration), within ~5 km, is  $105 \pm$   
472  $19$  °C, and a two-tailed Student's t-test indicates that the means are statistically different at the 99%  
473 confidence level. Qualitative observation of the Raman spectra corroborates the significant temperature  
474 difference between the eastern and western samples. The presence of significantly different Aoya  
475 temperatures in the east and west further corroborates this difference as these were derived using the  
476 same calibration and represent a degree of internal consistency. The temperatures are internally  
477 consistent within the western block, with the eastern block showing higher variation, particularly in the  
478 easternmost regions of the Northern Range. Samples in the east gradually increase in temperature from  
479 east to west, though they remain close to 340 °C. In addition, samples in the southwestern Northern  
480 Range are bounded by the Arima Fault and perhaps additional bounding faults, and typically show lower  
481 temperatures (350–410 °C) than their northwestern counterparts (~450 °C; Fig. 7a).

## 482 **6. Discussion**

### 483 **6.1 Metamorphic Field Gradient and Faulting**



484 Our RSCM data not only corroborate the existence of a geothermal gradient across the Northern  
485 Range, but now resolve that this gradient is discrete. The thermal discontinuity in the central Northern  
486 Range (Fig. 7a, b) juxtaposes high- ( $442 \pm 16$  °C) and low-temperature ( $337 \pm 10$  °C) blocks at Chupara  
487 Point. Given the abrupt temperature change we observe, a structural discontinuity must exist to  
488 accommodate it. The most probable candidate for such an intra-range boundary is the Chupara Fault as  
489 mapped by Kugler (1961) and De Verteuil et al. (2005). The Chupara Fault is one in a series of SE-  
490 striking normal faults that were hypothesized by Algar & Pindell (1993) to represent the final,  
491 transtensional stage of Northern Range deformation and presumed to be related to a change in the  
492 direction of Caribbean-South American plate motion from collisional to right-lateral strike-slip  
493 (transform).

494 Much of our RSCM data comes from the north coast, leaving the southern mountain front and  
495 internal segment of the metamorphic discontinuity more poorly constrained. Here, we refine slightly the  
496 Chupara Fault trace as mapped by De Verteuil et al. (2005), which was based on differences in  
497 metamorphic rock types and inferred differences in grade using microstructures. Topographic radar  
498 images show possible minor differences across the northern trace of the Chupara Fault; these diminish to  
499 the south (Fig. 7a), suggesting that the Chupara Fault is likely inactive. Future sampling in the range  
500 interior and more RSCM data can help to better define the position of the southern extent of the thermal  
501 gradient we observe as well as that of the Chupara Fault. We also note that we lack the data needed to  
502 speculate whether or how the onshore Chupara Fault relates to any offshore faults (e.g., Robertson and  
503 Burke, 1989).

504 In the southwestern Northern Range, the lower temperature samples of 350–410 °C in the  
505 Chancellor schist are separated from the main western block by a fault previously mapped by De  
506 Verteuil et al. (2005) (Fig. 7a). This fault may accommodate up to 4 km of vertical slip based on a

507 typical passive margin geotherm of 25 °C/km (Weber, Ferrill, et al., 2001). The temperature difference  
508 between the northwesternmost rocks and the Chancellor schist in the southwest mirrors the S–N grade  
509 increase observed in Paria, eastern Venezuela by Cruz et al. (2007, and references therein). Two samples  
510 ~3–5 km west of the Chupara Fault display slightly lower peak temperatures (~420 °C) than others  
511 surrounding them and thus may be separated from the rest of the western block by an additional splay  
512 fault(s) (e.g., Fig. 3b in Algar & Pindell, 1993) or some other unrecognized fault(s) (Fig. 2; De Verteuil  
513 et al., 2005). Finally, one outlier in the west, sample M-4, displays scattered, high peak temperatures of  
514  $497 \pm 27$ . This sample was collected from a shear zone where processes such as frictional heating during  
515 faulting may have altered the CM structure, leading to an increased RSCM-derived temperature  
516 (Furuichi et al., 2015).

517         The RSCM results from within the eastern block display an additional, less pronounced,  
518 systematic scatter (Fig. 7b), which might reflect second-order gradients or discontinuities that are  
519 difficult to quantify. This can be seen qualitatively by comparing the CM Raman spectra of samples  
520 from the eastern and central Northern Range (following, e.g., Kouketsu et al., 2014). We also note that  
521 the increased elongation of quartz grains in central metasandstones indicates a higher degree of quartz  
522 ductility and therefore, a potential for deeper burial and higher-grade metamorphism than rocks further  
523 east (Weber, Ferrill et al., 2001). Furthermore, the Sans Souci metabasalt (Fig. 2) along the northeast  
524 coast has a prehnite-pumpellyite mineral assemblage, while the rest of the eastern and central Northern  
525 Range appears to be mineralogically closer to or within the higher-grade greenschist facies (Frey et al.,  
526 1988). The RSCM data in the eastern block are sparse, so we are unable to rule out faulting as a cause of  
527 the potential eastern thermal gradient, and therefore further work is needed to confirm and more fully  
528 quantify the nature of this gradient.

## 529 **6.2 Timing of Metamorphism and Fault-related Exhumation**

530 We next used metamorphic ages and low-temperature thermochronology data, together with our  
531 RSCM results, to infer the timing of fault slip, differential bedrock cooling, and inferred exhumation  
532 along the block-bounding Chupara Fault. Our RSCM data provide new constraints and support for the  
533 previously proposed Miocene age of the Northern Range.  $^{40}\text{Ar}/^{39}\text{Ar}$  spectra from the Northern Range,  
534 introduced in abstract form (Foland et al., 1992) and in a field guide (Weber & Arkle, 2015) all indicate  
535 ages of ca. 25–30 Ma (Fig. 8b). In addition, Speed et al. (1997) determined the  $^{40}\text{Ar}/^{39}\text{Ar}$  age of well-  
536 ordered ( $10\text{\AA}$ ), syn-metamorphic white mica of the Dragon Gneiss in Paria, Venezuela, presenting an  
537 age of  $23.3 \pm 0.2$  Ma (between 8% and 95% Ar release). A second age in that study yielded a total gas  
538 age of 34.3 Ma with a plateau around 21 Ma (Speed et al., 1997). We note that the temperature estimates  
539 in other geothermometry studies ( $<400\text{ }^{\circ}\text{C}$ ; Frey et al., 1988; Weber, Ferrill, et al., 2001) are all lower  
540 than, or close to, the closure temperature of the muscovite  $^{40}\text{Ar}/^{39}\text{Ar}$  system ( $380 \pm 30\text{ }^{\circ}\text{C}$ ; Harrison et  
541 al., 2009). Because the  $^{40}\text{Ar}/^{39}\text{Ar}$  ages are mainly taken from metamorphic micas, previous studies  
542 regard them as representative of the timing of peak metamorphism. However, some of the younger ages  
543 (21–23 Ma) might have experienced Ar loss or resetting during cooling.

544 Zircon fission track (ZFT) data from the Northern Range show a general pattern with reset ages  
545 of  $\sim 12$  Ma in the west (Fig. 8b), whereas most eastern zircons are un-reset and display ages ranging  
546 from  $\sim 80$ – $200$  Ma (Algar et al., 1998; Arkle et al., 2021; Weber, Ferrill, et al., 2001). Our new RSCM  
547 temperatures from both the east and west ( $310$ – $450\text{ }^{\circ}\text{C}$ ) all exceed the ZFT closure temperature of  $240 \pm$   
548  $30\text{ }^{\circ}\text{C}$  (Brandon et al., 1998). This produces some discrepancy because of the presence of detrital ZFT  
549 ages at these temperatures; this relationship is also seen in studies of Taiwan's mountain ranges (Beyssac  
550 et al., 2007; Simoes et al., 2007). These discrepancies are thought to result from the complexities of  
551 zircon annealing, including effects related to variable thermal histories and a range of physical and  
552 chemical properties of zircon grains (Brandon et al., 1998).

553 Post-metamorphic thermochronology data from the Northern Range indicate significant  
554 differential exhumation of the eastern and western blocks between ~10–4.5 Ma (Arkle et al., 2021),  
555 which we suggest corresponds to the period of most active slip of the Chupara Fault (Fig. 8). Arkle et al.  
556 (2021) document rapid bedrock cooling and exhumation (~1.5 mm/yr) of the western Northern Range,  
557 wherein >7 km of rock was exhumed from ~10–4.5 Ma (Fig. 8b). During the same time period, thermal  
558 models indicate that pre-Pliocene exhumation of the eastern Northern Range was only <2 km (Fig. 8a).  
559 Although exhumation was clearly focused within the western and eastern crustal blocks of the Northern  
560 Range, mechanisms of differential exhumation such as discrete faults or other structures that dissect the  
561 mountain range could not previously be identified. We propose that the east-to-west offset of RSCM  
562 temperatures we observe need to be consistent with the magnitude and style of offset on the Chupara  
563 Fault. The 4 Ma–Recent differential exhumation between the eastern and western Northern Range could  
564 be accommodated by faulting, such as reactivation of the Chupara Fault. However, no geomorphic or  
565 geodetic evidence supports its Quaternary to Recent slip.

566 In the discussions above, we assume that cooling was mainly induced by exhumation. Evidence  
567 at the regional scale suggests that a majority of the differential cooling in the Northern Range can most  
568 reasonably be attributed to exhumation driven by normal faulting and erosion. Bedrock exhumation by  
569 erosion off the top of the North Range is supported by the initiation of high sedimentation rates in the  
570 Gulf of Paria basin starting at ~4 Ma and in the North Coast basin at ~12 Ma (Flinch et al., 1999). The  
571 late-stage normal faults pervasive throughout and surrounding the Northern Range (Algar & Pindell,  
572 1993; Kugler, 1961; Weber et al., 2015) also indicate favorability for fault-driven exhumation following  
573 peak burial. Furthermore, the timing of increased sedimentation, e.g., as described by Flinch et al.  
574 (1999), matches the timing of accelerated cooling in the west (late Miocene–Pliocene), suggesting a  
575 coupling between sedimentation and bedrock cooling due to erosional exhumation of the Northern

576 Range. On the other hand, Pindell and Kennan (2007) suggest that the underplating of cold proto-  
577 Caribbean material beneath the western Northern Range is responsible for its cooling (also see 6.3).  
578 However, this sort of regional-scale thermal conduction would presumably produce a more gradual  
579 temperature profile than that seen in our new RSCM data. In addition, such underthrusting is postulated  
580 to have occurred before the ~12 Ma Caribbean-South American collision in Trinidad (Algar & Pindell,  
581 1993; Pindell & Kennan, 2007). If underthrusting did cause significant cooling, its effect should  
582 therefore have been strongest before 12 Ma, precluding it from contributing significantly to the younger  
583 thermal gradient that we observe. Advection of cold fluid can, in principle, also produce steep field  
584 gradients (e.g., Rogiers et al., 2014), though its durations are shorter ( $< 0.1$  Myr) and depths are typically  
585 much shallower ( $< 2$  km) than the  $t$ - $T$  histories documented herein.

### 586 **6.3 Mechanisms of Hinterland Metamorphism**

587 Most models attribute metamorphism and subsequent exhumation of the Northern Range, as well  
588 as of Venezuela's Cordillera de la Costa, to the oblique collision between the Caribbean and South  
589 American Plates (Algar & Pindell, 1993; Garciacaro et al., 2011; Pindell & Kennan, 2001; Robertson &  
590 Burke, 1989). It is also generally agreed upon that exhumation occurred in Trinidad in the mid-Miocene,  
591 although its mechanism is disputed (Algar & Pindell, 1993; Arkle et al., 2017; 2021; Clark et al., 2008;  
592 Cruz et al., 2007; Speed, 1985; Weber, Ferrill, et al., 2001). Our new RSCM temperature estimates  
593 exceed temperature estimates from all previous metamorphic studies in the Northern Range (300–350  
594 °C, Frey et al., 1988; 250–400 °C, Weber, Ferrill, et al., 2001). If attributed to depth, the higher  
595 metamorphic grades call for revision of tectonic models to accommodate deep burial; here, we suggest  
596 that the required deep burial likely occurred through 1) the incorporation of additional shelf sediments  
597 into the fold-thrust or accretionary wedge (e.g., Pindell & Kennan, 2001), and 2) transpression acting to

598 squeeze this material between the two plates, allowing for both increased crustal thickness and orogenic  
599 uplift (e.g., Cruz et al., 2007).

600 The Northern Range rocks likely began as a mixture of passive margin (metamorphosed  
601 mudstone and turbidites) and continental shelf (becoming marbles and metasandstones) sedimentary  
602 protoliths (Fig. 9a). The sequence was incorporated into a fold-thrust wedge along the leading edge of  
603 the Caribbean plate with varying degrees of transport having been inferred (Fig. 9b; Pindell and Kennan,  
604 2001, 2007; Speed, 1985). The two end-members contrasting oblique collision models depict the entire  
605 south Caribbean metamorphic hinterland, including the Northern Range, either as an allochthon  
606 (Audemard, 2009; Avé Lallemant, 1997; Pindell & Kennan, 2001) or a parautochthon (Cruz et al., 2007;  
607 Russo & Speed, 1992, 1994).

608 Tomographic imaging beneath northern South America reveals a sinking mass, which has been  
609 associated with either a southward-subducting proto-Caribbean plate (Pindell and Kennan, 2001, 2007)  
610 or the removal of South American lithosphere along a near vertical crustal STEP (Levandar et al., 2014).  
611 The allochthonous model attributes deformation to events occurring since the early Paleocene due to the  
612 subduction of a proto-Caribbean plate beneath South America. Pindell and Kennan (2007) suggest that  
613 the Northern Range represents the accretion of both proto-Caribbean and Caribbean trench sediments.  
614 However, no magmatism associated with the southward subduction of a proto-Caribbean lithosphere  
615 beneath South America has been found on the South American continent. The lack of upper-plate  
616 volcanism and differing seismic tomographic interpretations leave the existence of a subducted proto-  
617 Caribbean plate open to debate (Levander et al., 2014; Pindell & Kennan, 2001, 2007). In addition, the  
618 accretionary model (Pindell & Kennan, 2001, 2007) requires about 200 km of displacement since 10 Ma  
619 to bring the Northern Range to its current position. This value contrasts with <100 km of displacement  
620 along the El Pilar and associated transform plate boundary faults (Audemard, 2009, and references

621 therein). We also note that the 450 °C temperature from our new RSCM results suggests deeper burial  
622 than is typical for both sedimentary and structural burial within accretionary wedges. In addition, the  
623 lack of high-pressure minerals like sodic-calcic amphiboles and garnet rules out potential high-P/T  
624 metamorphism of an oceanic slab such would be expected from the subduction of a large, mature  
625 “proto-Caribbean” plate. Thus, we prefer a model with significant crustal shortening associated with  
626 tectonic burial and crustal downflow to bring the Northern Range protoliths down to depths of ~17 km  
627 (25 °C/ km geotherm; c.f. Cruz et al., 2007), although we cannot rule out the possibility of some pre-  
628 collisional influence from a proto-Caribbean plate.

629 Cruz et al. (2007) suggest that the Venezuelan metamorphic belt was exhumed as a two-sided  
630 wedge, such as those described in the numerical models of Willet et al. (1993); as the Northern Range  
631 represents an extension of this belt, the same mechanism may apply. The geometry of a two-sided  
632 wedge (e.g., Cruz et al. 2007) could have been induced in Trinidad by northward subduction of the pre-  
633 collisional oceanic portion of the South American plate beneath the Caribbean plate. The model is  
634 supported by the oblique-normal shear indicators and SW-plunging lineations observed in the Cordillera  
635 de la Costa, Venezuela (Cruz et al., 2007). In a two-sided wedge, the material is accreted in the foreland  
636 and moves towards the retro-wedge of the hinterland, and thus, the metamorphic grade increases  
637 towards the retro-wedge (Willett et al., 1993). Topographically, a two-sided wedge presents a low-angle  
638 taper on the “pro-wedge” portion on the side of the subducting slab, while the “retro-wedge” is on the  
639 side of the overriding plate and displays a high-angle taper (Willet et al., 1993). The RSCM data from  
640 the southwestern Northern Range are consistent with this model, which predicts a metamorphic  
641 temperature increase towards the retro-wedge. The Chancellor schist displays lower RSCM temperatures  
642 than those in the rest of the western block (340–410 °C, purple unit in Fig. 7a). The range-front position  
643 of the Chancellor schist, and the fault-bounded, low-grade Laventille metalimestone and Lopinot

644 phyllite (Fig. 2), which display a range-front fold geometry of upright NE-SW trending folds, could  
645 reflect the modified southern side of a bivergent wedge (e.g., De Verteuil et al., 2005; Teyssier et al.,  
646 2002; Weber, Ferrill, et al. 2001). Farther south in the Central Range, which represents a major foreland  
647 fold-thrust structural culmination, <4 km of exhumation occurred from 18–11 Ma (Giorgis et al., 2017).  
648 Crustal shortening, development of a deep crustal root, and the deformation of the South American  
649 margin (Cruz et al., 2007), likely produced the observed metamorphic grades and significant burial  
650 depths of the Northern Range rocks (Fig. 9b). In sum, the lithological, structural, and thermal data of the  
651 Northern Range are all consistent with a two-sided wedge model and collision mechanism.

652         The bedrock cooling models of Arkle et al. (2021) indicate that a significant amount of post-  
653 collisional cooling and exhumation occurred in the western Northern Range from ~10–4.5 Ma, while  
654 little cooling and exhumation occurred in the east during that same time period. Arkle et al. (2021)  
655 further speculate that the STEP edge passed eastward under Trinidad following oblique collision (Fig.  
656 9c), creating a series of late-stage, en echelon normal faults that accommodated the overall strike-slip  
657 (transform) motion that is also pervasive throughout the Northern Rin Trinidad (Algar & Pindell, 1993;  
658 De Verteuil et al., 2005) and eastern Venezuela (Cruz et al., 2007). We propose that the Chupara Fault  
659 may be such a post-orogenic, extensional feature (Figs. 2, 7a, 9c). Thus, the activity of the Chupara  
660 Fault may be linked to the exhumation of the deeply buried rock in the western Northern Range that we  
661 document using RSCM data, perhaps as the STEP front migrated eastward (Fig. 9c). Thermal models,  
662 erosion data, and other regional geomorphic data also indicate that differential cooling and exhumation  
663 inverted around 4.5 Ma (Arkle et al., 2017: 2021). The STEP edge at this time (~4.5 Ma) would have  
664 moved sufficiently far to the east, became insignificant in the Northern Range, and brought the activity  
665 along the Chupara Fault to an end (Fig. 9d).

## 666 7. CONCLUSIONS



667 RSCM geothermometry provides important constraints on the peak metamorphic temperatures of  
668 key lithologic units across the Northern Range and helps to fill vital gaps in our understanding of its  
669 thermal history. The RSCM data collected across a broad swath of the range reveals a discrete thermal  
670 gradient with peak metamorphic temperatures of  $337 \pm 10$  °C in the east and  $442 \pm 16$  °C in the west,  
671 confirming the field gradient proposed by Frey et al. (1988) and demonstrated by Weber, Ferrill, et al.  
672 (2001). The abrupt temperature discontinuity of  $105 \pm 19$ °C located at Chupara Point corresponds to the  
673 location of the previously mapped Chupara Fault. Further field work is required to better constrain the  
674 precise location, timing, and kinematics of the Chupara Fault. Our new RSCM temperature estimates  
675 surpass all previous estimates and thus require greater burial depths of Northern Range rock. We  
676 speculate that Miocene oblique plate motion created a two-sided wedge in which parautochthonous  
677 Northern Range rocks were incorporated into a fold-thrust hinterland wedge. Our new peak  
678 temperatures, together with thermochronological data, lead us to interpret that the Chupara Fault is  
679 likely the main structure that accommodated differential exhumation between the eastern and western  
680 Northern Range. The distinctly different cooling trajectories suggest that the Chupara Fault was likely  
681 active from ~10–4.5 Ma, though activity before or after this time period cannot be completely ruled out.

## 682 **Acknowledgments**

683 This study was inspired by a departmental field trip to the Caribbean, organized and led by  
684 Professor Emeritus Edward Spooner and Laurent de Verteuil, along with undergraduate students Colin  
685 Roth and Jason Hinde. The Raman analyses and training at the University of Turin were supported by an  
686 Undergraduate Student Research Award of the Natural Sciences and Engineering Research Council  
687 (NSERC USRA, reference number 501984) to I.G. and a MIUR grant Levi Montalcini to A.V.B. The  
688 study is also supported by NSERC (Discovery Grant RGPIN-2018-03925 to X.C.). This work is part of  
689 a project that has received funding from the European Research Council (ERC) under the European

690 Union's Horizon 2020 research and innovation programme (Grant agreement No. 864045). We thank  
691 Veronica DiCecco and Yanan Liu for help with Raman spectroscopy and the electron microprobe  
692 analysis, at the Royal Ontario Museum and the University of Toronto respectively. Sample collection by  
693 Adam Brudner is gratefully acknowledged.

694

695

696

## 697 **References**

- 698 Algar, S. T., & Pindell, J. L. (1993). Structure and deformation history of the Northern Range of  
699 Trinidad and adjacent areas. *Tectonics*, 12(4), 814–829. <https://doi.org/10.1029/93TC00673>
- 700 Algar, S. T., Hady, E. C., & Pindell, J. L. (1998). Fission-track dating in Trinidad: Implications for  
701 provenance, depositional timing and tectonic uplift. In Pindell, J. L., & Drake, C. (Eds.),  
702 *Paleogeographic evolution and non-glacial eustasy, northern South America* (Special Publication 58,  
703 pp. 111–128). Tulsa, OK: Society of Economic Paleontologists and Mineralogists.
- 704 Anovitz, L. M., & Essene, E. J. (1987). Phase Equilibria in the System  $\text{CaCO}_3\text{-MgCO}_3\text{-FeCO}_3$ .  
705 *Petrology*, 28(2), 389–414. [https://doi.org/10.2473/shigentosozai1953.98.1131\\_441](https://doi.org/10.2473/shigentosozai1953.98.1131_441)
- 706 Aoya, M., Kouketsu, Y., Endo, S., Shimizu, H., Mizukami, T., Nakamura, D., & Wallis, S. (2010).  
707 Extending the applicability of the Raman carbonaceous-material geothermometer using data from  
708 contact metamorphic rocks. *Journal of Metamorphic Geology*, 28, 895–914.  
709 <https://doi.org/10.1111/j.1525-1314.2010.00896.x>
- 710 Arkle, J. C., Owen, L. A., Weber, J. C., Caffee, M. W., & Hammer, S. (2017). Transient Quaternary  
711 erosion and tectonic inversion of the Northern Range, Trinidad. *Geomorphology*, 295, 337–353.  
712 <https://doi.org/10.1016/j.geomorph.2017.07.013>
- 713 Arkle, J. C., Weber, J. C., Enkleman, E., Owen, L. A., Govers, R., Denison, C., et al. (2021).  
714 Exhumation of the coastal metamorphic belt above a subduction-to-transform transition, in the southeast  
715 Caribbean plate corner. *Tectonics*, 40(8). <https://doi.org/10.1029/2020TC006414>
- 716 Audemard, F. A. (2009). Key issues on the post-Mesozoic Southern Caribbean Plate boundary.  
717 *Geological Society Special Publication*, 328, 569–586. <https://doi.org/10.1144/SP328.23>
- 718 Avé Lallemant, H. G. (1997). Transpression, displacement partitioning, and exhumation in the eastern  
719 Caribbean / South American plate boundary zone. *Tectonics*, 16(2), 272–289.  
720 <http://dx.doi.org/10.1029/96TC03725>
- 721 Babb, S. and Mann, P. (1999). Structural and sedimentary development of a Neogene transpressional  
722 plate boundary between the Caribbean and South American plates in Trinidad and the Gulf of Paria. In

723 Mann, P., ed., *Caribbean basins: Sedimentary basins of the world* (Volume 4, pp. 495–557).  
 724 Amsterdam, Netherlands: Elsevier Science B.V.

725 Barr, K.W. (1965). The Geology of the Toco District, Trinidad, West Indies, Pt. I and II. Overseas  
 726 Geology and Mineral resources, 8, 4, 379-415 and 9, 1, 1-29.

727 Bartlett, C., Arkle, J., Weber, J. and Erlich, R. (2021). Provenance of the Northern Range Trinidad  
 728 Using Detrital Zircon U-Pb Geochronology: Implications for Northern South American River System  
 729 Paleogeography, Geological Society of America, North-Central Meeting.

730 Bayet, L., John, T., Agard, P., Gao, J., & Li, J. (2018). Massive sediment accretion at ~80 km depth  
 731 along the subduction interface: Evidence from the southern Chinese Tianshan. *Geology*, 46(6), 495–498.  
 732 <https://doi.org/10.1130/G40201.1>

733 Beyssac, O., Goffé, B., Chopin, C., & Rouzaud, J. N. (2002). Raman spectra of carbonaceous material in  
 734 metasediments: a new geothermometer. *Journal of Metamorphic Geology*, 20, 859–871.  
 735 <https://doi.org/10.1046/j.1525-1314.2002.00408.x>

736 Beyssac, O., Goffé, B., Petitet, J. P., Froigneux, E., Moreau, M., & Rouzaud, J. N. (2003). On the  
 737 characterization of disordered and heterogeneous carbonaceous materials by Raman spectroscopy.  
 738 *Spectrochimica Acta - Part A: Molecular and Biomolecular Spectroscopy*, 59, 2267–2276.  
 739 [https://doi.org/10.1016/S1386-1425\(03\)00070-2](https://doi.org/10.1016/S1386-1425(03)00070-2)

740 Beyssac, O., & Lazzeri, M. (2012). Application of raman spectroscopy to the study of graphitic carbons  
 741 in the earth sciences. *European Mineralogical Union Notes in Mineralogy*, 12(12), 415–454.  
 742 <https://doi.org/10.1180/EMU-notes.12.12>

743 Beyssac, O., Pattison, D. R. M., & Bourdelle, F. (2019). Contrasting degrees of recrystallization of  
 744 carbonaceous material in the Nelson aureole, British Columbia and Ballachulish aureole, Scotland, with  
 745 implications for thermometry based on Raman spectroscopy of carbonaceous material. *Journal of*  
 746 *Metamorphic Geology*, 37, 71–95. <https://doi.org/10.1111/jmg.12449>

747 Beyssac, O., Simoes, M., Avouac, J. P., Farley, K. A., Chen, Y. G., Chan, Y. C., & Goffé, B. (2007).  
 748 Late Cenozoic metamorphic evolution and exhumation of Taiwan. *Tectonics*, 26(6).  
 749 <https://doi.org/10.1029/2006TC002064>

750 Brandon, M. T., Roden-Tice, M. K., & Carver, J. I. (1998). Late Cenozoic exhumation of the Cascadia  
 751 accretionary wedge in the Olympic Mountains, northwest Washington State. *Bulletin of the Geological*  
 752 *Society of America*, 110(8), 985–1009. [https://doi.org/10.1130/0016-](https://doi.org/10.1130/0016-7606(1998)110<0985:LCEOTC>2.3.CO;2)  
 753 [7606\(1998\)110<0985:LCEOTC>2.3.CO;2](https://doi.org/10.1130/0016-7606(1998)110<0985:LCEOTC>2.3.CO;2)

754 Burke, K. (1988). Tectonic evolution of The Caribbean. *Annual Reviews in Earth and Planetary Science*,  
 755 16, 201–230. <https://doi.org/10.1146/annurev.earth.16.050188.001221>

756 Clark, S. A., Sobiesiak, M., Zelt, C. A., Magnani, M. B., Miller, M. S., Bezada, M. J., & Levander, A.  
 757 (2008). Identification and tectonic implications of a tear in the South American plate at the southern end  
 758 of the Lesser Antilles. *Geochemistry, Geophysics, Geosystems*, 9(11), 1–10.  
 759 <https://doi.org/10.1029/2008GC002084>

760 Cruz, L., Fayon, A., Teyssier, C., & Weber, J. C. (2007). Exhumation and deformation processes in  
761 transpressional orogens: The Venezuelan Paria Peninsula, SE Caribbean-South American plate  
762 boundary. *Special Paper of the Geological Society of America*, 434(8), 149–165.  
763 [https://doi.org/10.1130/2007.2434\(08\)](https://doi.org/10.1130/2007.2434(08))

764 De Verteuil, L., Weber, J. C., Ramlal, B., & Gonzalez Alfonso, J. A. (2005). *Geological Map of*  
765 *Trinidad*. Republic of Trinidad and Tobago: Latinum Geological Consultants Limited.

766 Dighton-Thomas, H. (1935). On some sponges and a coral of Upper Cretaceous Age from Toco Bay,  
767 Trinidad, *Geological Magazine*, 72, 4, 175–179.

768

769 Flinch, J. F., Rambaran, V., Ali, W., De Lisa, V. De, Hernández, G., Rodrigues, K., & Sams, R. (1999).  
770 Structure of the Gulf of paria pull-apart basin (Eastern Venezuela-Trinidad). In Mann, P., (Ed.)  
771 *Sedimentary Basins of the World* (Vol. 4, pp. 477–494). Frisco CO: Elsevier Science.  
772 [https://doi.org/10.1016/S1874-5997\(99\)80051-3](https://doi.org/10.1016/S1874-5997(99)80051-3)

773 Foland, K. A., Speed, R., & Weber, J. C. (1992). Geochronologic studies of the hinterland of the  
774 Caribbean orogen of Venezuela and Trinidad. *Geological Society of America Abstracts with Programs*,  
775 24, 148.

776 Furuichi, H., Ujiie, K., Kouketsu, Y., Saito, T., Tsutsumi, A., Wallis, S. (2015). Vitritite reflectance and  
777 Raman spectra of carbonaceous material as indicators of frictional heating on faults: Constraints from  
778 friction experiments. *Earth and Planetary Letters*, 424, 191–200.  
779 <https://doi.org/10.1016/j.epsl.2015.05.037>

780 Frey, M., Saunders, J., & Schwander, H. (1988). The mineralogy and metamorphic geology of low-  
781 grade metasediments, Northern Range, Trinidad. *Journal of the Geological Society, London*, 145, 563–  
782 575. <https://doi.org/10.1144/gsjgs.145.4.0563>

783 Garciacaro, E., Mann, P., & Escalona, A. (2011). Regional structure and tectonic history of the obliquely  
784 colliding Columbus foreland basin, offshore Trinidad and Venezuela. *Marine and Petroleum Geology*,  
785 28, 126–148. <https://doi.org/10.1016/j.marpetgeo.2009.08.016>

786 Gennaro, I., Chu, X., Vitale Brovarone, A., Weber, J., Arkle, J. (2021). Peak metamorphic temperatures  
787 aquired through Raman Spectroscopy on Carbonaceous Material (RSCM) from the Northern Range,  
788 Trinidad. PANGAEA, <https://doi.pangaea.de/10.1594/PANGAEA.932772>

789 Giorgis, S., Weber, J. C., Sanguinito, S., Beno, C., & Metcalf, J. (2017). Thermochronology constraints  
790 on miocene exhumation in the central range mountains, Trinidad. *Bulletin of the Geological Society of*  
791 *America*, 129(1–2), 171–178. <https://doi.org/10.1130/B31363.1>

792 Govers, R., & Wortel, M. J. R. (2005). Lithosphere tearing at STEP faults: Response to edges of  
793 subduction zones. *Earth and Planetary Science Letters*, 236(1–2), 505–523.  
794 <https://doi.org/10.1016/j.epsl.2005.03.022>

795 Harrison, T. M., Célrier, J., Aikman, A. B., Hermann, J., & Heizler, M. T. (2009). Diffusion of <sup>40</sup>Ar in  
796 muscovite. *Geochimica et Cosmochimica Acta*, 73(4), 1039–1051.  
797 <https://doi.org/10.1016/j.gca.2008.09.038>

798 Hoernle, K., Hauff, F., & van den Bogaard, P. (2004). 70 m.y. history (139–69 Ma) for the Caribbean  
799 large igneous province. *Geology*, 32(8), 697–700. <https://doi.org/10.1130/G20574.1>

800 Imlay, R.W. (1954). Barremian ammonites from Trinidad, B.W.I., *Journal of Paleontology*, 28, 5, 662-  
801 667.

802 Iwasaki, R., Hirose, M., & Furukawa, Y. (2013). Raman temperature measurements of copper  
803 phthalocyanine layer of organic light-emitting diode using bandwidth-temperature relationship.  
804 *Japanese Journal of Applied Physics*, 52(5S1), 05DC16.

805 Kagi, H., Tsuchida, I., Wakatsuki, M., Takahashi, K., Kamimura, N., Iuchi, K., & Wada, H. (1994).  
806 Proper understanding of down-shifted Raman spectra of natural graphite: Direct estimation of laser-  
807 induced rise in sample temperature. *Geochimica et Cosmochimica Acta*, 58(16), 3527-3530.

808 Kirlova, M., Toy, V., Rooney, J. S., Giorgetti, C., Gordon, K. C., Collettini, C., Takeshita, T. (2018).  
809 Structural disorder of graphite and implications for graphite thermometry. *Solid Earth*, 9, 223–231.  
810 <https://doi.org/10.5194/se-9-223-2018>

811 Kugler, H. G. (1961). *Geological map and sections of Trinidad*. Zurich, Switzerland: Orell Füssli Arts  
812 Graphiques S. A.

813 Kennan, L., & Pindell, J. L. (2009). Dextral shear, terrane accretion and basin formation in the Northern  
814 Andes: Best explained by interaction with a Pacific-derived Caribbean plate? *Geological Society Special  
815 Publication*, 328, 487–531. <https://doi.org/10.1144/SP328.20>

816 Kouketsu, Y., Mizukami, T., Mori, H., Endo, S., Aoya, M., Hara, H., et al. (2014). A new approach to  
817 develop the Raman carbonaceous material geothermometer for low-grade metamorphism using peak  
818 width. *Island Arc*, 23, 33–50. <https://doi.org/10.1111/iar.12057>

819 Lahfid, A., Beyssac, O., Deville, E., Negro, F., Chopin, C., & Goffé, B. (2010). Evolution of the Raman  
820 spectrum of carbonaceous material in low-grade metasediments of the Glarus Alps (Switzerland). *Terra  
821 Nova*, 22(5), 354–360. <https://doi.org/10.1111/j.1365-3121.2010.00956.x>

822 Levander, A., Bezada, M. J., Niu, F., Humphreys, E. D., Palomeras, I., Thurner, S. M., et al. (2014).  
823 Subduction-driven recycling of continental margin lithosphere. *Nature*, 515, 253–256.  
824 <https://doi.org/10.1038/nature13878>

825 Lünsdorf, N. K., Dunkl, I., Schmidt, B. C., Rantitsch, G., & von Eynatten, H. (2013). Towards a Higher  
826 Comparability of Geothermometric Data obtained by Raman Spectroscopy of Carbonaceous Material.  
827 Part I: Evaluation of Biasing Factors. *Geostandards and Geoanalytical Research*, 38(1), 73–94.  
828 <https://doi.org/10.1111/j.1751-908X.2013.12011.x>

829 Luque, F. J., Pasteris, J. D., Wopenka, B., Rodas, M., & Barrenechea, J. F. (1998). Natural Fluid-  
830 Deposited Graphite: Mineralogical Characteristics and Mechanisms of Formation. *American Journal of  
831 Science*, 298(6), 471–498. <https://doi.org/10.2475/ajs.298.6.471>

832 Molli, G., Vitale Brovarone, A., Beyssac, O., & Cinquini, I. (2018). RSCM thermometry in the Alpi  
833 Apuane (NW Tuscany, Italy): New constraints for the metamorphic and tectonic history of the inner  
834 northern Apennines. *Journal of Structural Geology*, 113, 200–216.  
835 <https://doi.org/10.1016/j.jsg.2018.05.020>

836 Nakamura, Y., Hara, H., & Kagi, H. (2019). Natural and experimental structural evolution of dispersed  
837 organic matter in mudstones: The Shimanto accretionary complex, southwest Japan. *Island Arc*, 28(5),  
838 e12318.

839 Nakamura, Y., Oohashi, K., Toyoshima, T., Satish-Kumar, M., Akai, J. (2015). Strain-induced  
840 amorphization of graphite in fault zones of the Hidaka metamorphic belt, Hokkaido, Japan. *Journal of*  
841 *Structural Geology*, 72, 142–161. <https://doi.org/10.1016/j.jsg.2014.10.012>

842 Neill, I., Kerr, A., Chamberlain, K. R., Schmitt, A. K., Urbani, F., Hastie, A. R. et al. (2014). Vestiges of  
843 the proto-Caribbean seaway: Origin of the Sans Souci volcanic group, Trinidad. *Tectonophysics*, 626,  
844 170–185. <https://doi.org/10.1016/j.tecto.2014.04.019>

845 Nijholt, N., & Govers, R. (2015). The role of passive margins on the evolution of Subduction-Transform  
846 Edge Propagators (STEPS). *Journal of Geophysical Research: Solid Earth*, 120, 7203–7230.  
847 <https://doi.org/10.1002/2015JB012202>

848 Pindell, J., & Kennan, L. (2001). Processes and Events in the Terrane Assembly of Trinidad and Eastern  
849 Venezuela. In *Petroleum Systems of Deep-Water Basins: Global and Gulf of Mexico Experience: 21st*  
850 *Annual* (159–192). Red Hook, NY: Curran Associates Inc. <https://doi.org/10.5724/gcs.01.21.0159>

851 Pindell, J. & Kennan, L. (2007). Cenozoic Kinematics and Dynamics of Oblique Collision Between two  
852 Convergent Plate Margins: The Caribbean-South America Collision in Eastern Venezuela, Trinidad and  
853 Barbados. In *Transactions of GCSSEPM 27<sup>th</sup> Annual Bob F. Perkins Research Conference*, 458–553.  
854 <https://doi.org/10.5724/gcs.07.27.0458>

855 Pindell, J. & Kennan, L. (2009). Tectonic evolution of the Gulf of Mexico, Caribbean and northern  
856 South America in the mantle reference frame: an update. In *Geological Society London, Special*  
857 *Publications*, 328, 1–55. <https://doi.org/10.1144/SP328.1>

858 Potter, H. C. (1968). A preliminary account of the stratigraphy and structure of the eastern part of the  
859 Northern Range, Trinidad. In *Transactions of the Fourth Caribbean Geological Conference*, Trinidad,  
860 15–20.

861 Potter, H. C. (1973). The overturned anticline of the Northern Range of Trinidad near Port of Spain.  
862 *Journal of the Geological Society*, 129, 133–137. <http://dx.doi.org/10.1144/gsjgs.129.2.0133>

863 Rahl, J. M., Anderson, K. M., Brandon, M. T., & Fassoulas, C. (2005). Raman spectroscopic  
864 carbonaceous material thermometry of low-grade metamorphic rocks: Calibration and application to  
865 tectonic exhumation in Crete, Greece. *Earth and Planetary Science Letters*, 240(2), 339–354.  
866 <https://doi.org/10.1016/j.epsl.2005.09.055>

867 Robertson, P., & Burke, K. (1989). Evolution of southern Caribbean plate boundary, vicinity of Trinidad  
868 and Tobago. *American Association of Petroleum Geologists Bulletin*, 73(4), 490–509.  
869 <https://doi.org/10.1306/44b49fdd-170a-11d7-8645000102c1865d>

870 Rogiers, B., Huysmans, M., Vandenberghe, N., Verkeyn, M. (2014). Demonstrating large-scale cooling  
871 in a Variscan terrane by coupled groundwater and heat flow modelling. *Geothermics*, 51, 71–90.  
872 <http://dx.doi.org/10.1016/j.geothermics.2013.10.014>

873 Rumble, D. (2014). Hydrothermal graphitic carbon. *Elements*, 10(6), 427–433.  
874 <https://doi.org/10.2113/gselements.10.6.427>

875 Russo, R. M., & Speed, R. C. (1992). Oblique collision and tectonic wedging of the South American  
876 continent and Caribbean terranes. *Geology*, 20(5), 447–450. [https://doi.org/10.1130/0091-](https://doi.org/10.1130/0091-7613(1992)020<0447:OCATWO>2.3.CO;2)  
877 [7613\(1992\)020<0447:OCATWO>2.3.CO;2](https://doi.org/10.1130/0091-7613(1992)020<0447:OCATWO>2.3.CO;2)

878 Russo, R. M., & Speed, R. C. (1994). Spectral analysis of gravity anomalies and the architecture of  
879 tectonic wedging, NE Venezuela and Trinidad. *Tectonics*, 13(3), 613–622.  
880 <https://doi.org/10.1029/94TC00052>

881 Simoes, M., Avouac, J. P., Beyssac, O., Goffé, B., Farley, K. A., & Chen, Y. G. (2007). Mountain  
882 building in Taiwan: A thermokinematic model. *Journal of Geophysical Research: Solid Earth*, 112(11),  
883 1–25. <https://doi.org/10.1029/2006JB004824>

884 Saunders, J.B. (1972). Recent paleontological results from the Northern Range of Trinidad, Proceedings  
885 on the Sixth Caribbean Geological Conference, Caracas, 455-460.

886 Saunders, J. B., Roberts, C., Ali, W. M., Eggerston, B. (1997). *Geological Map, Trinidad and Tobago*.  
887 Trinidad and Tobago: Ministry of Energy and Energy Resources.

888 Spath, L.F. (1939). On some Tithonian ammonites from the Northern Range of Trinidad, British West  
889 Indies Geological Magazine, 76, 898, 187-198.

890 Speed, R. C. (1985). Cenozoic Collision of the Lesser Antilles Arc and Continental South America and  
891 the Origin of the El Pilar Fault. *Tectonics*, 4(1), 41–69. <https://doi.org/10.1029/TC004i001p00041>

892 Speed, R.C., Sharp, W.D., and Foland, K.A., (1997). Late Paleozoic granitoid gneiss of northeastern  
893 Venezuela and the North American-Gondwana collision zone, *Journal of Geology*, 105(4), 457–470.

894 Teyssier, C., Tikoff, B., Weber, J. (2002). Attachment between brittle and ductile crust at wrenching  
895 plate boundaries. *EGU Stephan Mueller Special Publication Series*, 1, 75–91.

896 Trechmann, C.T. (1935). Fossils from the Northern Range of Trinidad, *Geological Magazine*, 72, 850,  
897 166-175.

898 Vitale Brovarone, A., & Agard, P. (2013). True metamorphic isograds or tectonically sliced  
899 metamorphic sequence? New high-spatial resolution petrological data for the New Caledonia case study.  
900 *Contributions to Mineralogy and Petrology*, 166(2), 451–469. [https://doi.org/10.1007/s00410-013-0885-](https://doi.org/10.1007/s00410-013-0885-2)  
901 2

902 Vitale Brovarone, A., Beyssac, O., Malavieille, J., Molli, G., Beltrando, M., & Compagnoni, R. (2013).  
903 Stacking and metamorphism of continuous segments of subducted lithosphere in a high-pressure wedge:  
904 The example of Alpine Corsica (France). *Earth-Science Reviews*, 116(1), 35–56.  
905 <https://doi.org/10.1016/j.earscirev.2012.10.003>

906 Wadge, G & Macdonald, R. (1985). Cretaceous tholeiites of the southern continental margin of South  
907 America: the Sans Souci Formation of Trinidad. *Journal of the Geological Society of London*, 142, 297–  
908 308. <https://doi.org/10.1144/gsjgs.142.2.0297>

909 Wang, Y., Alsmeyer, D. C., McCreery, R. L. (1990). Raman spectroscopy of carbon materials:  
910 Structural basis of observed spectra. *Chemical Materials*, 2, 557–563.

911 Weber, J. C. (2009). Neotectonics in the Trinidad and Tobago, West Indies segment of the Caribbean-  
912 South American plate boundary. *Occasional Papers of the Geological Institute of Hungary*, 204, 21–29.

913 Weber, J. C., & Arkle, J. (2015). *Field Trip Field Guide Trinidad's Northern Range: "reversal of*  
914 *fortune": Bedrock Structure and Metamorphic Geology, and Tectonic Geomorphology*. Port-of-Spain,  
915 Trinidad: 20th Caribbean Geological Conference.

916 Weber, J. C., Dixon, T. H., DeMets, C., Ambeh, W. B., Jansma, P., Mattioli, G., et al. (2001). GPS  
917 estimate of relative motion between the Caribbean and South American plates, and geologic  
918 implications for Trinidad and Venezuela. *Geology*, 29(1), 75–78. [https://doi.org/10.1130/0091-](https://doi.org/10.1130/0091-7613(2001)029<0075:GEORMB>2.0.CO;2)  
919 7613(2001)029<0075:GEORMB>2.0.CO;2

920 Weber, J. C., Ferrill, D. A., & Roden-Tice, M. K. (2001). Calcite and quartz microstructural  
921 geothermometry of low-grade metasedimentary rocks, Northern Range, Trinidad. *Journal of Structural*  
922 *Geology*, 23(1), 93–112. [https://doi.org/10.1016/S0191-8141\(00\)00066-3](https://doi.org/10.1016/S0191-8141(00)00066-3)

923 Weber, J. C., H. Geirsson, J. L. Latchman, K. Shaw, P. La Femina, S. Wdowinski, M. Higgins, C.  
924 Churches, and E. Norabuena (2015), Tectonic inversion in the Caribbean-South American plate  
925 boundary: GPS geodesy, seismology, and tectonics of the Mw 6.7 22 April 1997 Tobago earthquake,  
926 *Tectonics*, 34, 1181–1194, doi:10.1002/2014TC003665.

927 Weber, J. C., Geirsson, H., La Femina, P., Robertson, R., Churches, C., Shaw, K., et al. (2020). Fault  
928 Creep and Strain Partitioning in Trinidad-Tobago: Geodetic Measurements, Models, and Origin of  
929 Creep. *Tectonics*, 39(1), e2019TC005530. <https://doi.org/10.1029/2019TC005530>

930 Willett, S., Beaumont, C., & Fullsack, P. (1993). Mechanical model for the tectonics of doubly vergent  
931 compressional orogens. *Geology*, 21(4), 371–374. [https://doi.org/10.1130/0091-](https://doi.org/10.1130/0091-7613(1993)021<0371:MMFTTO>2.3.CO;2)  
932 7613(1993)021<0371:MMFTTO>2.3.CO;2

933 Wopenka, B., & Pasteris, J. D. (1993). Structural characterization of kerogens to granulite-facies  
934 graphite: Applicability of Raman microprobe spectroscopy. *American Mineralogist*, 78(5–6), 533–557.

935

936



**Table 1. Rock Type, Location, and RSCM Temperatures of Northern Range Samples**

Sample	Spectro- meter	Lithology	UTM X coordinate <sup>a</sup>	UTM Y coordinate <sup>a</sup>	5-Peak Spectra Temperature (SE) <sup>f</sup>		3-Peak Spectra Temperature (SE) <sup>g</sup>		RSCM Temperature (SE) <sup>e</sup>		FWHM-D1 Temperature (SE) <sup>h</sup>		FWHM-D2 Temperature (SE) <sup>h</sup>	
DT-93-1 <sup>b</sup>	-	Phyllite	672200	1189900	-	-	-	-	-	-	-	-	-	-
145	UNITO	Schist	672500	1178400			348	2.9	<b>348</b>	<b>2.9</b>	362	3.6	277	18.3
HT-161	ROM	Phyllite	672500	1178400	341	4.0	355	2.1	<b>347</b>	<b>4.7</b>	360	3.4	383	3.6
CF-94-1	ROM	Marble	672698	1178373			353	1.8	<b>353</b>	<b>1.8</b>	367	2.6	332	6.8
T94-3	ROM	Slate	723638	1198298	325	4.4			<b>325</b>	<b>4.4</b>	287	5.0	320	1.1
T97- MAT3	ROM	Slate	706235	1196714	339	2.9			<b>339</b>	<b>2.9</b>	298	2.1	322	0.9
M-3	UNITO	Schist	671697	1189674	<i>1 outlier</i>		461	4.7	<b>461</b>	<b>4.7</b>	-	-	-	-
	ROM	Schist	671697	1189674			447	3.6	<b>447</b>	<b>3.6</b>	-	-	-	-
M-4	UNITO	Schist	671697	1189674	<i>1 outlier</i>		497	7.9	<b>497</b>	<b>7.9</b>	-	-	-	-
	ROM	Schist	671697	1189674			492	10.6	<b>492</b>	<b>10.6</b>	-	-	-	-
Ar-17	ROM	Metasandstone	683682	1193264	364	3.9			<b>364</b>	<b>3.9</b>	334	3.5	310	3.6
LC-91a	UNITO	Metasandstone	675697	1192174			413	3.6	<b>413</b>	<b>3.6</b>	-	-	-	-
T90-9b	ROM	Phyllite	672820	1178826			340	1.4	<b>340</b>	<b>1.4</b>	354	3.1	298	7.1
LN-94-1	UNITO	Metacarbonate	721934	1197921	327	3.1			<b>327</b>	<b>3.1</b>	243	5.3	256	11.7
	ROM	Metacarbonate	721934	1197921	272	3.5			<b>272</b>	<b>3.5</b>	270	5.8	292	9.1
SC-2	UNITO	Marble	666223	1185430			465	8.6	<b>465</b>	<b>8.6</b>	-	-	-	-
T94-1	UNITO	Metacarbonate	723497	1198074	322	2.7			<b>322</b>	<b>2.7</b>	227	7.9	323	5.5
	ROM	Metacarbonate	723497	1198074	302	2.5			<b>302</b>	<b>2.5</b>	245	3.5	360	3.5
SC-2b	UNITO	Marble	669482	1189870	<i>1 outlier</i>		449	4.1	<b>449</b>	<b>4.1</b>	-	-	-	-
MV-94-3	ROM	Metacarbonate	717297	1197675	310	3.5			<b>310</b>	<b>3.5</b>	263	1.6	319	7.2
PG-94-5 <sup>c</sup>	ROM	Metacarbonate	650597	1180273			315 <sup>c</sup>		<b>315<sup>c</sup></b>		314 <sup>c</sup>		287 <sup>c</sup>	
93-T-CB	UNITO	Marble	679302	1194346	<i>3 outliers</i>		366	4.6	<b>366</b>	<b>4.6</b>	354	2.4	248	8.9
MAT-1	ROM	Slate	704866	1196982	341	4.1	<i>1 outlier</i>		<b>341</b>	<b>4.1</b>	292	3.2	320	3.7
CB-2a	UNITO	Marble	678698	1195474	348 <sup>d</sup>		344	1.2	<b>344</b>	<b>1.2</b>	349	2.1	233	10.9
	ROM	Marble	678698	1195474			341	1.4	<b>341</b>	<b>1.4</b>	366	2.3	302	5.8
DT-93	UNITO	Schist	672763	1189887			454	2.9	<b>454</b>	<b>2.9</b>	-	-	-	-
	ROM	Schist	672763	1189887			453	3.3	<b>453</b>	<b>3.3</b>	-	-	-	-
MB-93-1	ROM	Schist	650900	1187570			444	5.2	<b>444</b>	<b>5.2</b>	-	-	-	-
LC-91b	UNITO	Schist	676033	1192116			422	3.9	<b>422</b>	<b>3.9</b>	-	-	-	-
LC-3	ROM	Phyllite	661869	1180984			410	2.2	<b>410</b>	<b>2.2</b>	-	-	-	-
NR-1	UNITO	Metasandstone	720092	1185918			338	0.3	<b>337</b>	<b>2.2</b>	343	2.0	244	7.2
	ROM	Metasandstone	720092	1185918	336	4	341	1.1	<b>342</b>	<b>1.1</b>	355	1.5	287	3.8
NR-2 (-5)	UNITO	Slate	724652	1192884	351	1.5	340	***	<b>350</b>	<b>4.5</b>	311	1.9	311	4.1
NR-3 (-1)	UNITO	Metasandstone	720092	1185918	327	1.3	335	0.3	<b>329</b>	<b>3.7</b>	318	5.5	174	10.8

939 <sup>a</sup> UTM coordinates are in Zone 20.  
940 <sup>b</sup> Sample DT-93-1 was unable to be analyzed due to a lack of carbonaceous material.  
941 <sup>c</sup> Sample PG-94-5 has a temperature based on one spectrum as all other spectra collected contained large calcite peaks and could  
942 not be fit accurately.  
943 <sup>d</sup> One spectrum only.  
944 <sup>e</sup> These temperatures are calculated using the Aoya et al. (2010) or Lahfid et al. (2010) calibrations. In samples displaying both 3-  
945 and 5-band spectra both calibrations were used, with the reported value representing the average temperature of all spectra  
946 associated with that sample (exculding outliers). Consult the supplementary material for a full breakdown of the calibrations used  
947 for each spectrum.  
948 <sup>f</sup> Aoya et al. (2010).  
949 <sup>g</sup> Lahfid et al. (2010).  
950 <sup>h</sup> Kouketsu et al. (2014).

951 **Figure Captions**

952

953 **Figure 1:** a) Schematic tectonic map of the eastern Caribbean showing major plate boundaries. Trinidad  
954 (grey) is currently located on the right-lateral strike-slip transform boundary along the southern edge of  
955 the Caribbean Plate. PC – Paria cluster of seismicity. b) Map of Trinidad emphasizing the Northern  
956 Range study area (grey) and major faults in the region. The active faults (Central Range and Los Bajos  
957 faults, bold lines) accommodate most of the present plate motion between the Caribbean and South  
958 America (Weber, Dixon, et al., 2001). The Northern Range is bound by the inactive North Coast and  
959 Sub-Tobago Terrane fault zones to the north and Arima Fault to the south. The El Pilar Fault zone is  
960 active in eastern Venezuela but is inactive or not present in Trinidad. c) Cross section of the subduction-  
961 transform edge propagator (STEP) plate boundary and associated lithospheric tear located below the  
962 Caribbean Plate. The subduction-transform boundary is located at the letter “S” while the site of active  
963 and deep tearing is located at the Paia Cluster, which is a major zone of earthquakes in the area as a  
964 result of the slab tear (Russo & Speed, 1992). Modified after Arkle et al. (2021).

965

966 **Figure 2:** Simplified geologic map from De Verteuil et al. (2005) of the Northern Range showing  
967 metamorphic units, sample localities, and relict fossil ages. Apart from the Sans Souci Metabasalt, all  
968 lithologic units are metamorphosed from sedimentary protoliths (Frey et al., 1988), with relict fossil  
969 ages only available from eastern block, lower-grade units (Dighton-Thomas, 1935; Imlay, 1954; Kugler,  
970 1961; Saunders, 1972; Spath, 1939; Trechmann, 1935). A total of 26 RSCM samples were collected and  
971 grouped into six representative rock types. Sample distribution was based on obtaining a broad range of  
972 compositions and textures. PS – Port of Spain; CP – Chupara Point; VV – Verdant Vale; M – Maturita;  
973 T – Toco.

974

975 **Figure 3:** Photomicrographs of petrographic thin sections displaying representative features of each  
976 rock type. a) calcite (Cal) marble with carbonaceous material (Gr) concentrated into dark bands; b)  
977 calcite (Cal) vein in a metacarbonate rock indicating late extensional brittle deformation and infilling via  
978 precipitation from a CO<sub>2</sub>-rich fluid; c) low-grade metacarbonate marble displaying primary sedimentary  
979 structures (ooids) which have been moderately strained by ductile deformation but have not been  
980 recrystallized; d) quartz-mica (Qz-Ms) schist with foliation and minor calcite, likely representing a  
981 sandstone protolith; e) mica-rich (Ms) phyllite displaying crenulation after multiple deformation events;  
982 f) radial growth of carbonaceous material (CM) superimposed on schistosity; g) metasandstone with  
983 minor chlorite (Chl), muscovite, and quartz (Qz); h) folded quartz (Qz)- and CM (Gr)-rich layers in a  
984 metasandstone; i) slate rich in carbonaceous material, quartz (Qz), and mica (Ms). PPL: plane-polarized  
985 light, XPL: cross-polarized light, RL: reflected light.

986

987 **Figure 4:** a) Backscattered electron (BSE) image of a foliated slate. The dolomite (dol) in the sample  
988 has a euhedral shape whereas the calcite (cc) appears more subhedral-anhedral, indicating a lack of  
989 equilibrium between the two phases. Pyrite (py) framboids are also present. b) CaCO<sub>3</sub>-MgCO<sub>3</sub>-FeCO<sub>3</sub>

phase diagrams calculated for different temperatures (Anovitz & Essene, 1987), with carbonate compositions plotted in red.

**Figure 5:** Peak-fitted Raman spectra of (a) high- and (b) low- temperature samples. The high-temperature spectra are fit with Voigt bands while Lorentzian bands are used for the low-temperature spectrum; the area ratios between these bands are used to calculate the peak metamorphic temperature of a sample (Aoya et al., 2010; Lahfid et al., 2010). c) Raman spectra showing decreasing band complexity, correlating to increasing crystallinity and peak metamorphic temperature, from bottom to top. The temperatures shown are calculated using the <sup>1</sup>Lahfid et al. (2010) and <sup>2</sup>Aoya et al. (2010) calibrations.

**Figure 6:** Inter-instrument error between Raman spectrometers at UNITO and the ROM. The low-temperature calibrations of Lahfid et al. (2010) and Kouketsu et al. (2014) show a lower reproducibility than the high-temperature calibration of Aoya et al. (2010). Inset: variability between the two calibrations of Kouketsu et al. (2014) which are up to 100 °C.

**Figure 7:** a) RSCM results given in °C plotted on a geologic map of Trinidad overlying topographic (radar) data. The abrupt temperature change in the central Northern Range is marked by a major lithologic boundary along the previously mapped Chupara Fault (Kugler, 1961; De Verteuil et al., 2005). The temperatures shown are calculated using the Aoya et al. (2010) and Lahfid et al. (2010) calibrations. b) Temperature ( $\pm 1$  s.e.) for samples along the north coast of the Northern Range calculated using a variety of RSCM calibrations. Lower temperature samples from the southwestern Chancellor Schist are excluded as they are separated from the higher temperature samples by the E-W trending Arima Fault. Average temperatures ( $1\sigma$ ) of the eastern and western blocks are displayed as the blue-shaded regions.

**Figure 8:** Cooling history of the a) eastern and b) western Northern Range modified from the QTQt bedrock cooling models of Arkle et al. (2021). Timing of peak metamorphism is estimated by <sup>40</sup>Ar/<sup>39</sup>Ar ages through the Northern Range (Speed et al., 1997, Weber & Arkle, 2015). In the east, the cooling path following peak metamorphic temperature, and possibly its timing, remains largely unconstrained due to the disparity between un-reset ZFT ages and high RSCM temperatures, potentially indicating a short-lived thermal event. Dark and light grey lines are the expected cooling histories of the high and low elevation samples, respectively, with the shaded regions representing a 95% confidence interval (Arkle et al., 2021).

**Figure 9:** Cartoon showing tectonic evolution of the Northern Range and Araya-Paria, Venezuela, metamorphic hinterland, modified from Arkle et al. (2021). a) Following Jurassic-Cretaceous rifting, the area was dominated by passive margin deposition of sediment along continental South America. b) Oblique plate collision led to peak metamorphism and thrust faulting in the Northern Range in the late Oligocene. This time marks the inception of foreland and hinterland structures and of hinterland

1028 metamorphism. c) A transition to strike-slip plate motion between the Caribbean and South American  
1029 plates produced structures such as the Gulf of Paria pull-apart basin. Eastward propagation of the STEP  
1030 edge induced greater exhumation of the western Northern Range upon its arrival in Trinidad, which was  
1031 accommodated by the Chupara Fault. d) Continued STEP propagation along the plate boundary led to an  
1032 inversion in Northern Range exhumation and late Pliocene to recent surface uplift, with subsidence  
1033 currently dominant in the west as the east experiences surface uplift (e.g., Arkle et al. 2017, 2021). NR –  
1034 Northern Range; SdI – Serranía del Interior; MB – Maturin Basin; CR – Central Range; SR – Southern  
1035 Range; CF – Chupara Fault; NCFZ – Northern Coastal fault zone; EPFZ – El Pilar Fault zone; CB –  
1036 Columbus Basin.

1037

1038 **Figure S1:** Plots of nominal temperatures calculated using 3- (Aoya et al., 2010; square symbols) and 5-  
1039 band (Lahfid et al., 2010; plus signs) calibrations against the centers of fitted G bands. The G band of  
1040 fully ordered graphite ( $1582\text{ cm}^{-1}$ ; Wang et al., 1990) is labeled by dashed lines for reference. The  
1041 analyses at UNITO and ROM are denoted by black and blue colors, respectively.

1042

Figure 1

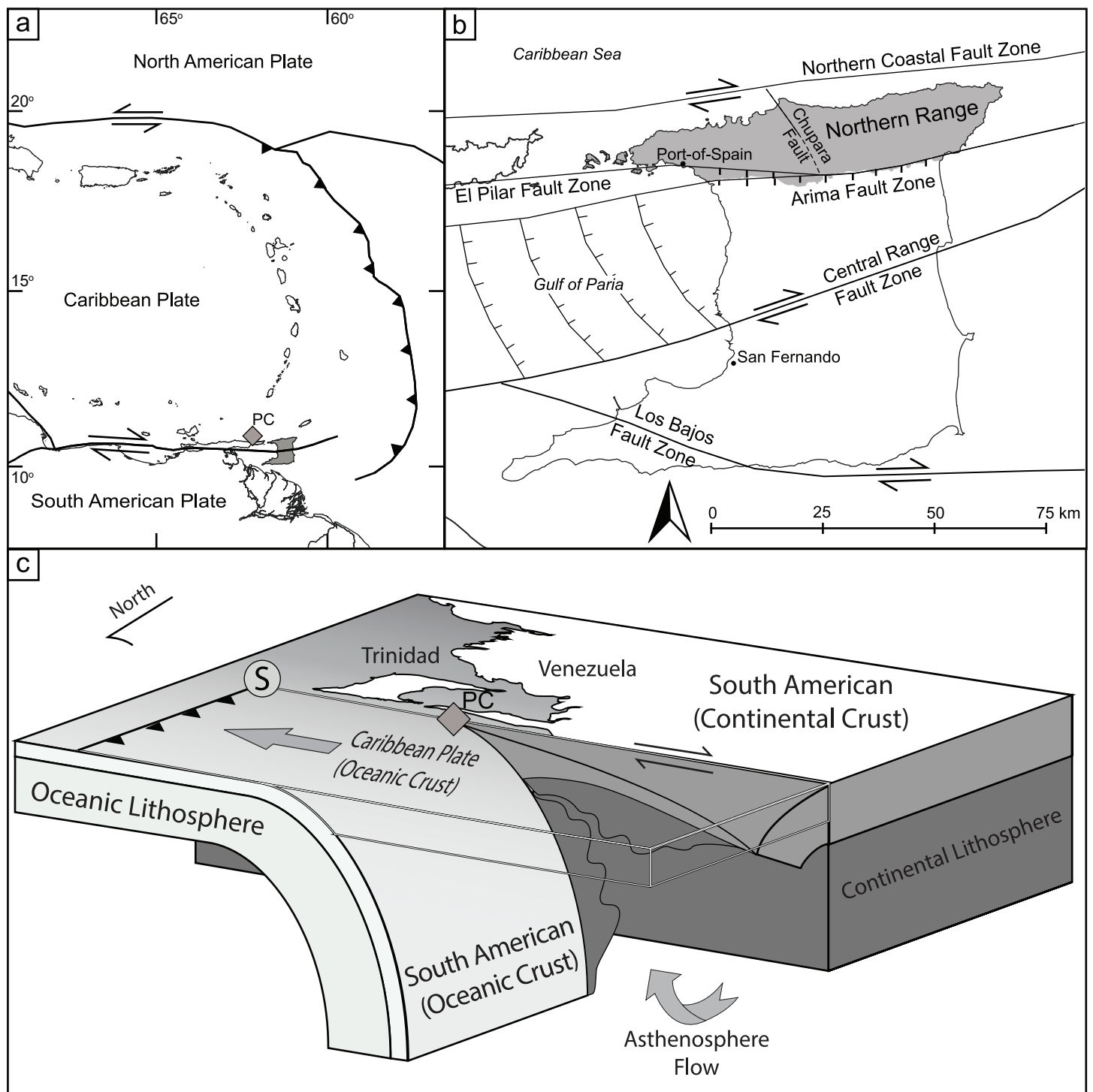


Figure 2

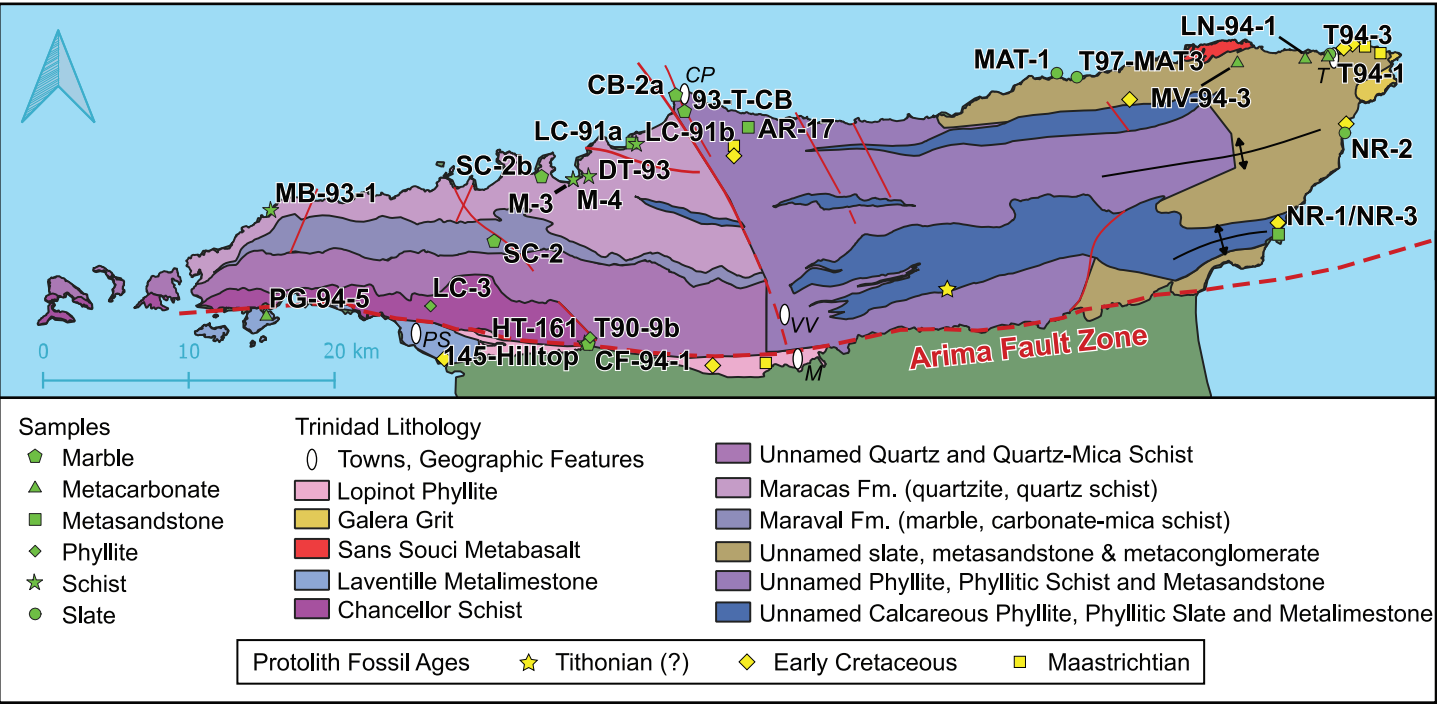


Figure 3

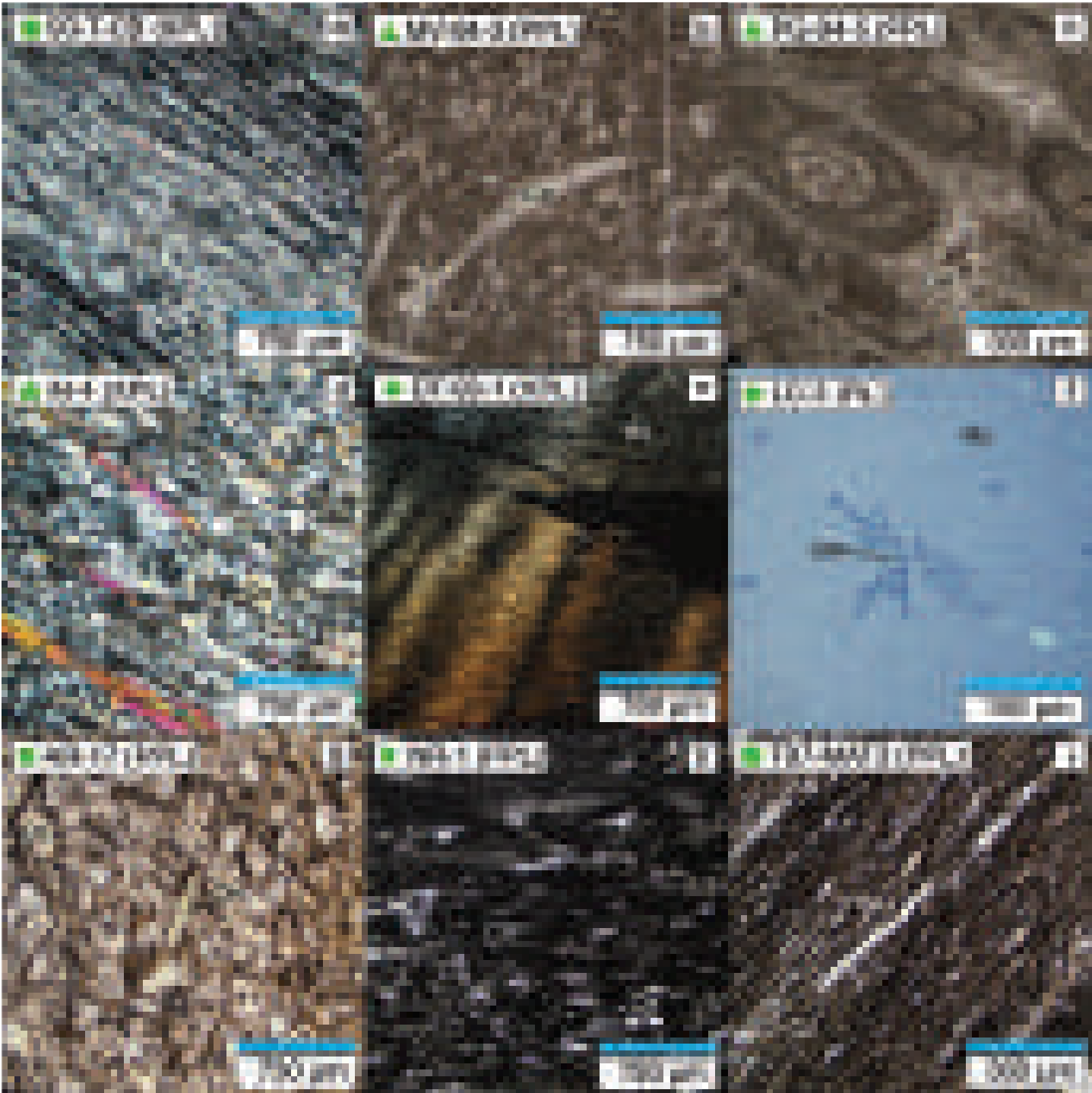




Figure 4

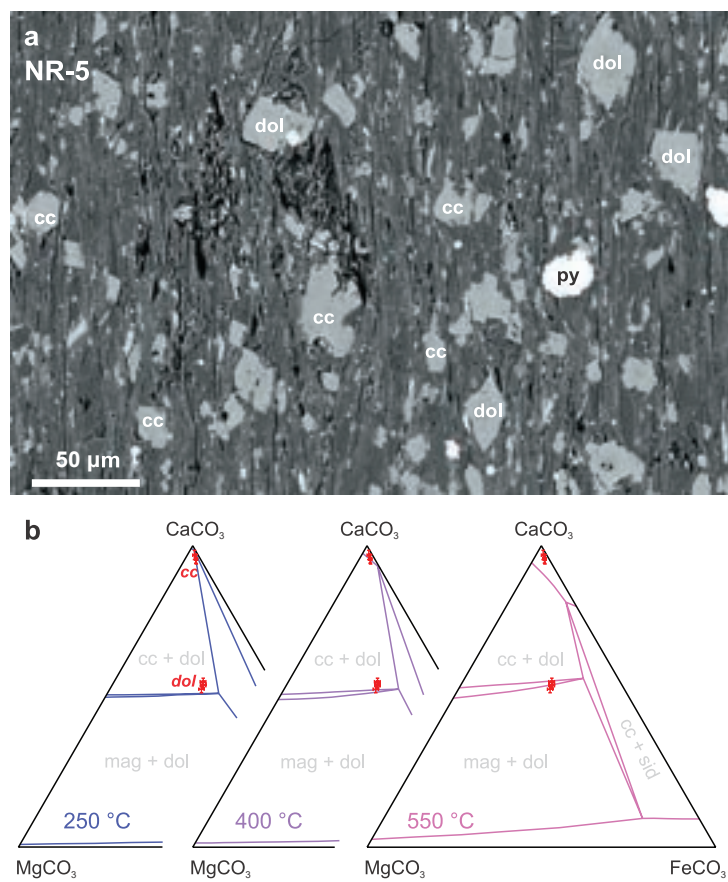


Figure 5

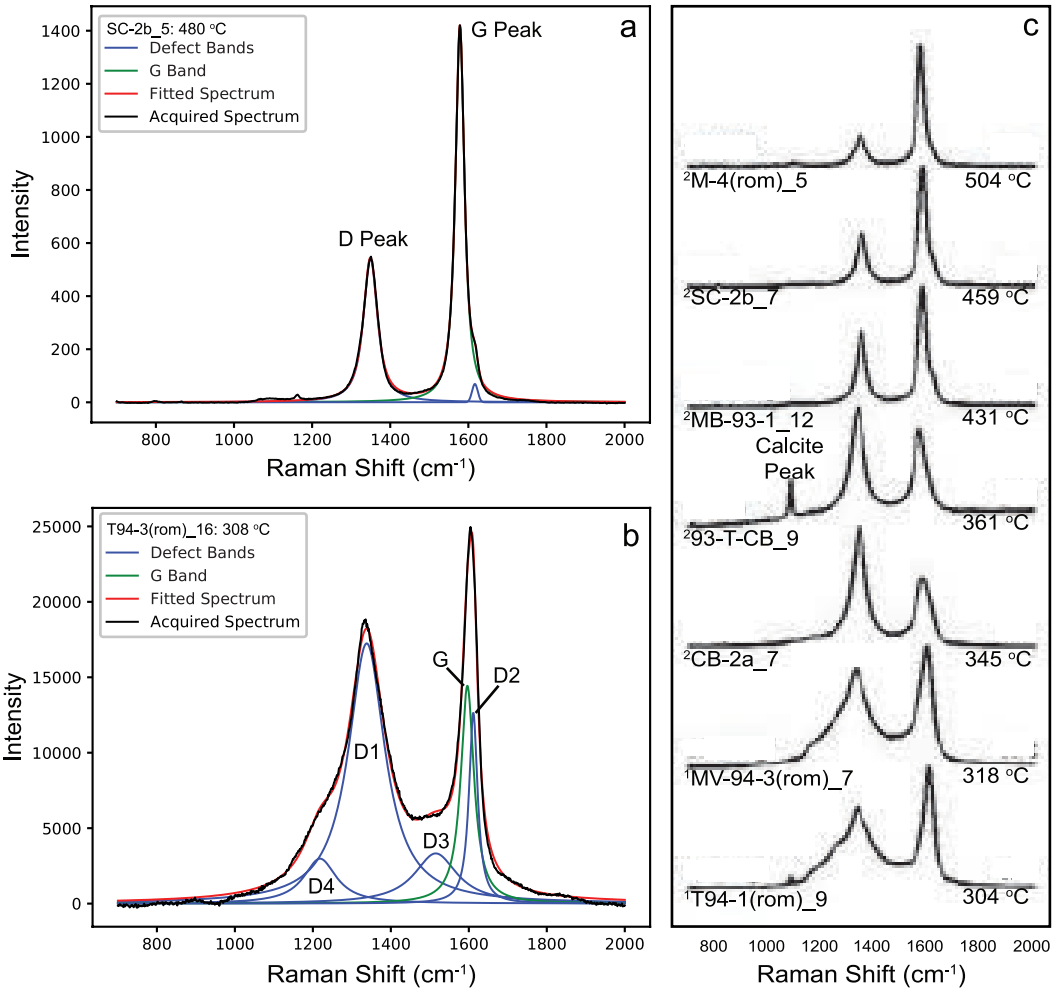


Figure 6

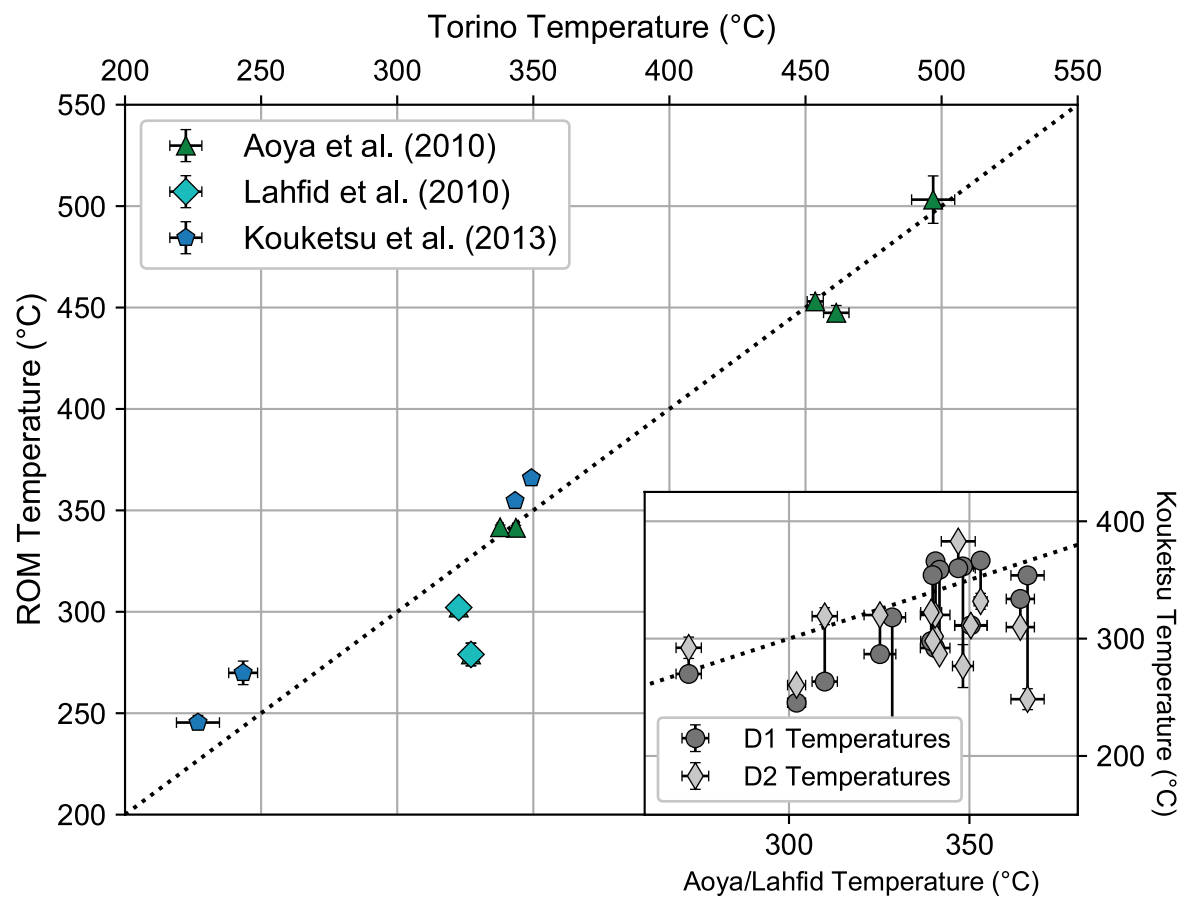


Figure 7

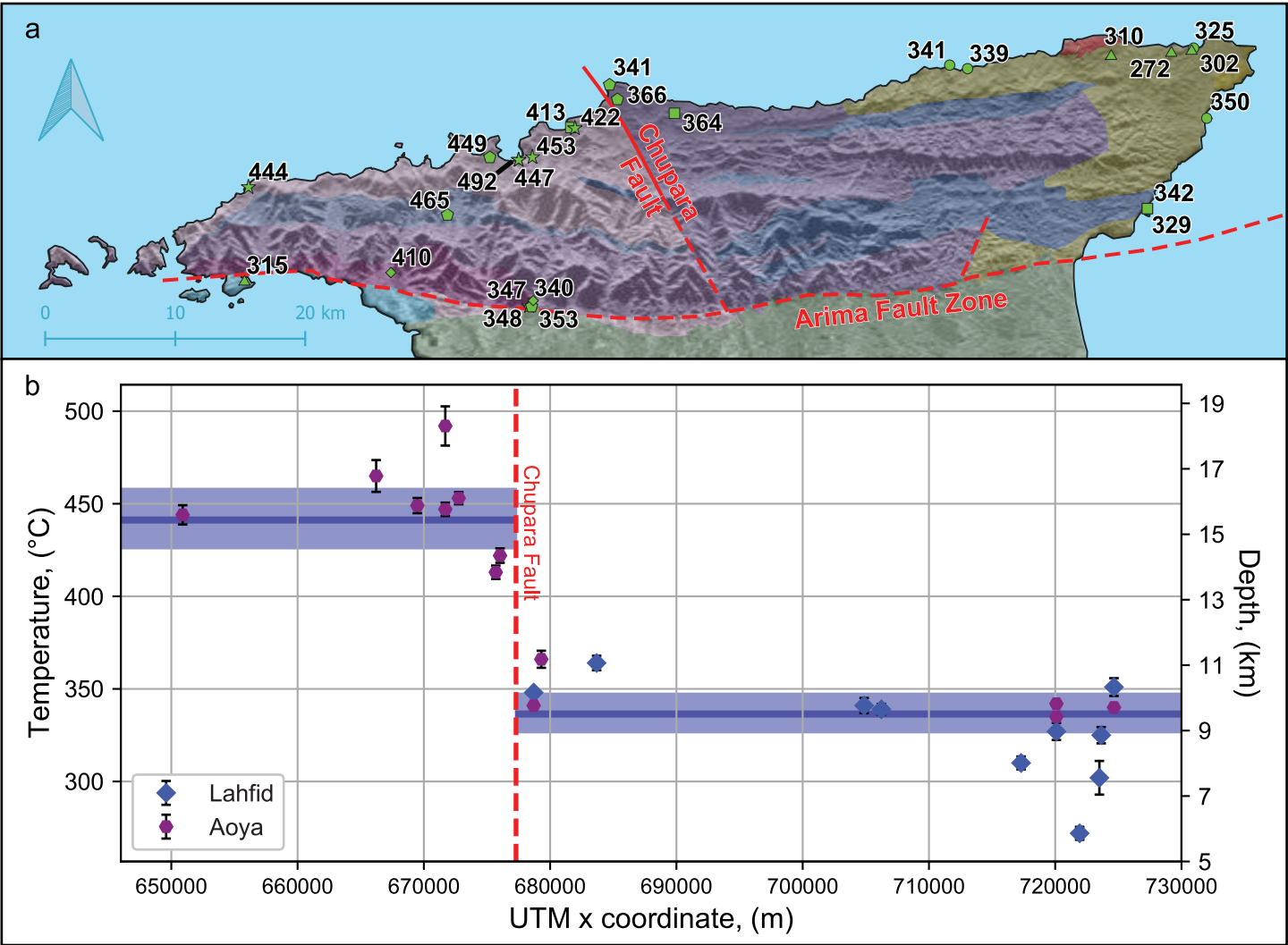


Figure 8

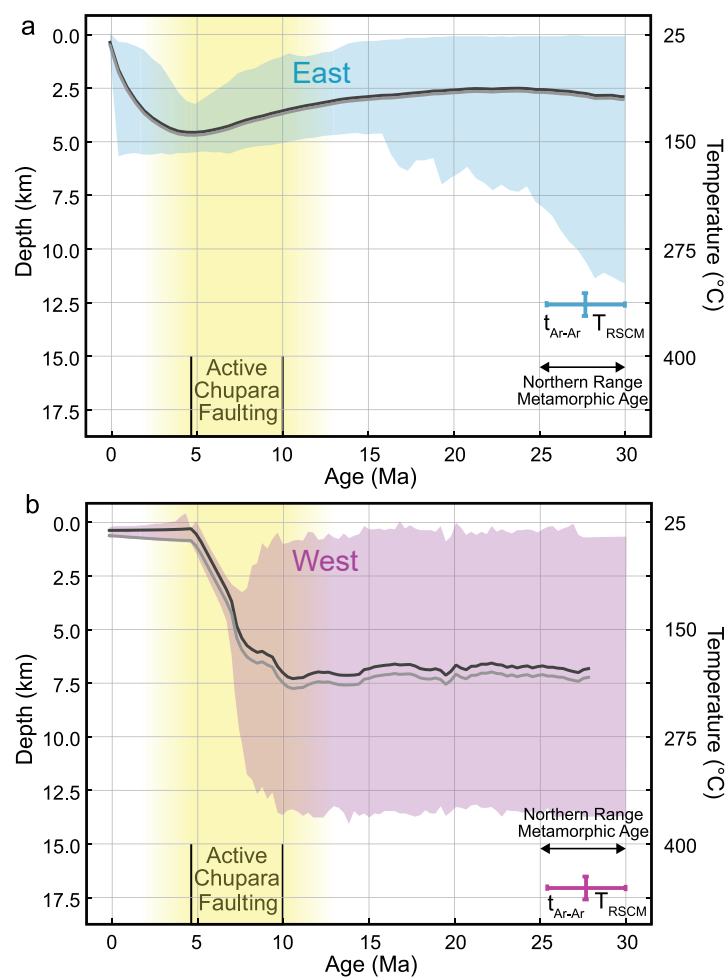


Figure 9

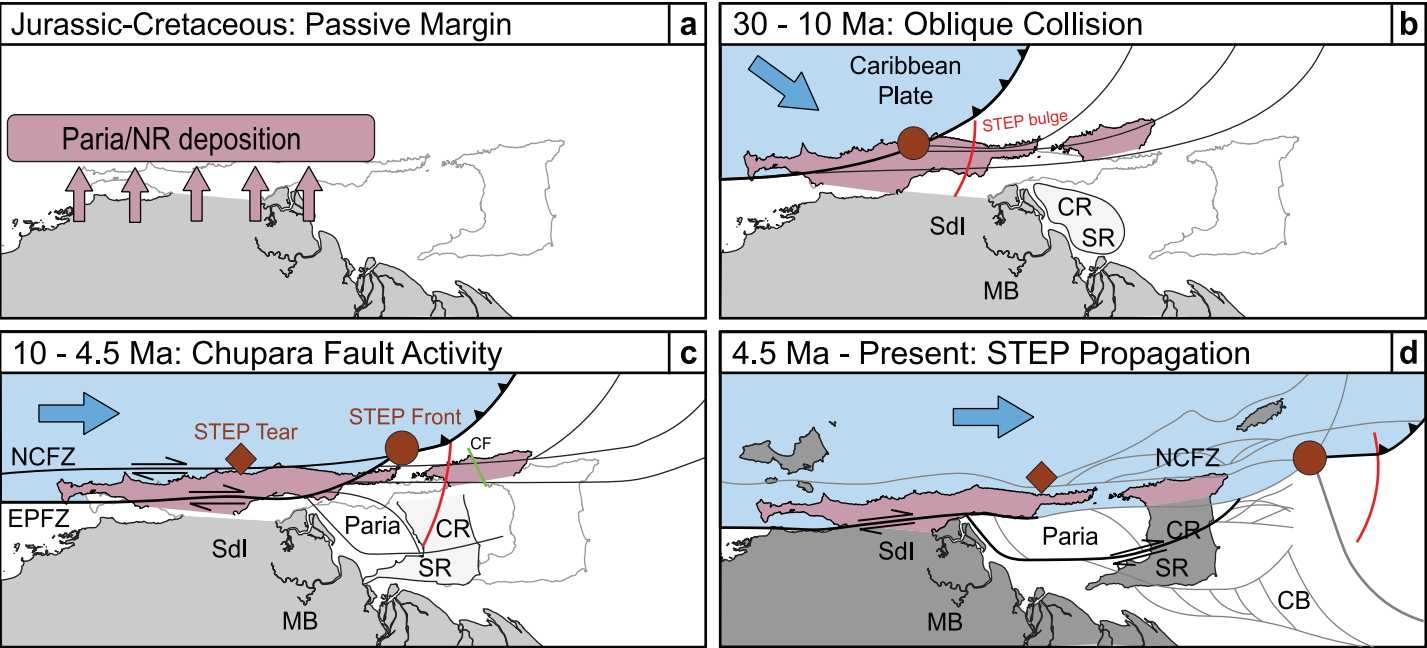


Figure S1

